

Appendix A

Free Parameters and Frameworks in Minimal Supersymmetry

It is useful to discuss what parameters of supersymmetric models are presently constrained or unconstrained by experiment and to delineate the various schemes that exist for reducing the set of free parameters to a manageable number. The information presented here is derived from discussions between Paolo Gondolo and Rick Gaitskell, Vuk Mandic, and myself.

The parameters fixed by experiment are the following:

- **h**: The quark and lepton mass and mixing matrices, also known as the Yukawa couplings because they define a Yukawa-type coupling to the Higgs, whose vacuum expectation value turns these into mass terms. Fixed by observed Standard Model particle masses and mixing.
- g_1, g_2, g_3 : The gauge couplings for the $U(1)$ hypercharge, $SU(2)$ electroweak, and $SU(3)$ strong interactions. They are fixed by the observed strengths of these interactions.
- $v_1^2 + v_2^2$: This quadrature sum of the vacuum expectation values of the two Higgs fields sets the mass of the W and Z weak bosons, and so is fixed by experiment.

The free parameters consist mainly of the coefficients of the “soft” supersymmetry-breaking terms in the Lagrangian. Obviously, supersymmetry must be broken to give the world we see, where no superpartners have yet been observed. However, the breaking must be done in such a way that the desirable traits of supersymmetry — in particular, cancellation of quadratic divergences above the SUSY-breaking scale — are preserved. This condition restricts the allowed breaking terms to a small set, first determined by Girardello and Grisaru [53]. Their coefficients are as follows:

- \mathbf{M}_f^2 : The sfermion masses. These are 3×3 hermitian matrices, one for each type of sfermion: $\widetilde{q}_L, \widetilde{u}_R^c, \widetilde{d}_R^c, \widetilde{l}_L, \widetilde{e}_R^c$, and $\widetilde{\nu}_R^c$ (assuming neutrinos are massive and thus that the normal particle ν_R exists!). Each matrix has 9 free parameters, giving a total of 54 free parameters. Note that these may be nondiagonal and therefore may themselves contribute to sfermion mixing, though this freedom has been accounted for in the above count.
- **A**: The sfermion-mixing matrices. These are three 3×3 matrices with no hermiticity requirement. There are therefore 18 free parameters per matrix, yielding a total of 54 free

parameters. There is a loose requirement that the minima of all the sfermions' scalar potentials (*i.e.*, the sum of all terms containing the powers of a given sfermion field alone, such as mass terms) be minimized at 0, but this constraint only puts some allowed range on the matrix components; it does not yield specific relations between components.

- M_1, M_2, M_3 : The gaugino masses. Three free parameters.
- $m_1^2, m_2^2, B, \tan \beta \equiv v_2/v_1, \mu$: Higgs parameters (supersymmetry and electroweak-symmetry breaking). m_1^2 and m_2^2 are real scalars. B is a scalar and may be complex. $\tan \beta$ is limited by experiment from below and by m_t/m_b from above. Of these, three can be taken to be free and the others determined via the electroweak-symmetry breaking relations. Choices of parameter sets are
 - $m_1^2, m_2^2, \tan \beta$ free, B and μ dependent ([51], Equation 69).
 - B, μ , and $\tan \beta$ free, m_1^2 and m_2^2 dependent ([51], Equation 68).
 - $m_A^2 = -2B\mu/\sin 2\beta, \tan \beta, \mu$ free, B, m_1^2 , and m_2^2 dependent. (m_A^2 is the mass of the pseudoscalar Higgs boson). A new non-independent quantity, m_A^2 , has been introduced, so there are now three dependent parameters instead of two. The reason for this choice is that m_A^2 is a more physical parameter. This is what is used in most numerical codes. It should be noted that these conditions hold even for radiative electroweak-symmetry breaking — radiative EWSB imposes an additional condition.

Summing up the above, there are a total of 115 free parameters! There are different schemes for reducing the above freedom; these different schemes are called “frameworks,” to distinguish them from a “model,” which consists of a specific choice for all the parameters.

- **mSUGRA**: Short for *minimal supergravity* — this framework assumes that, above the Planck scale (10^{19} GeV), supersymmetry can be gauged: the invariance under global supersymmetry transformations can be promoted to invariance under local supersymmetry transformations. This yields general relativity, since supersymmetry transformations are related to Lorentz transformations. Some mechanism breaks this local invariance at energies below the Planck scale. However, since the GUT scale (10^{16} GeV) is so much lower, there is no reason to expect this mechanism to distinguish between the different gauge groups and particle generations. Thus, mSUGRA yields the maximal set of assumptions:
 - Gaugino-mass unification: $M_1 = M_2 = M_3 \equiv m_{1/2}$ at M_{GUT} .
 - Fermion Yukawa-coupling unification: $\mathbf{h}_E = \mathbf{h}_U = \mathbf{h}_D \equiv \mathbf{h}$ at M_{GUT} .
 - Sfermion-mass and -mixing unification: $\mathbf{M}_l^2 = \mathbf{M}_q^2 = \mathbf{M}_e^2 = \mathbf{M}_{\bar{\nu}}^2 = \mathbf{M}_u^2 = \mathbf{M}_d^2 = m_1^2 \mathbf{1} = m_2^2 \mathbf{1} \equiv m_0^2 \mathbf{1}$ and $\mathbf{A}_e = \mathbf{A}_u = \mathbf{A}_d \equiv A_0 \mathbf{1}$ at M_{GUT} .
 - $B = A_0 + m_0$ at M_{GUT} .
 - Some specification of the GUT gauge group. This is necessary to determine the running of the couplings from the Planck scale to the GUT scale.
 - Radiative electroweak-symmetry breaking: the electroweak-symmetry breaking parameters are generated by higher-order diagrams that can be summed into an effective Higgs potential. The parameters of the potential are thus set by other parameters and are not

free. This provides another relationship between μ^2 and the other Higgs sector parameters, thereby adding another condition and reducing the number of free parameters in the Higgs sector to two (usually taken to be m_A^2 , the pseudoscalar mass, and $\tan\beta$).

This framework is the most constraining one available. It is not used, however, because some of its consequences violate observations. These will be noted below as more free frameworks are defined.

- **mSUGRA_{LHC}/mSUGRA_{LEP}**: This is what is meant when LEP data or LHC expectations are discussed in the context of “minimal supergravity.” A few assumptions are relaxed:
 - Yukawa-coupling unification is not required. It is impossible to unify the first and second generation couplings at the GUT scale and still yield reasonable masses at observed energies. The first and second generation coupling unification is thus released immediately. mSUGRA_{LHC}/mSUGRA_{LEP} also release the 3rd generation — this is also known as “no b/τ mass unification” for obvious reasons.
 - Radiative electroweak-symmetry breaking is employed, but, when picking models, no checks are made on the color/charge neutrality of the vacuum for the given set of parameters.
- **Generic SUGRA**: Releases assumptions further:
 - No Higgs-sfermion-mass unification. The two Higgs masses are assumed to be unified, $m_1^2 = m_2^2$. It is usually m_A^2 that is specified, which is related to these by EWSB. All the sfermion masses are assumed to be unified, $\mathbf{M}_l^2 = \mathbf{M}_q^2 = \mathbf{M}_e^2 = \mathbf{M}_\nu^2 = \mathbf{M}_u^2 = \mathbf{M}_d^2 \equiv m_0^2 \mathbf{1}$. Lack of Higgs-sfermion-mass unification allows $m_{1,2}^2 \neq m_0^2$ at M_{GUT} .
 - No radiative electroweak-symmetry breaking — standard spontaneous electroweak-symmetry breaking is assumed, so there are three free Higgs parameters, as discussed earlier.

The release of Higgs-sfermion-mass unification is done for three reasons. First, it allows one to separate the Higgs and sfermion sectors (the sleptons and squarks are linked by the sfermion-mass unification relation at the GUT scale), sending one or the other to very high mass to simplify analysis of models. Second, the gauge couplings do not unify properly at M_{GUT} if Higgs-sfermion-mass unification is enforced. Finally, superstring theories suggest there really is no connection between the Higgs and sfermion masses.

- **Constrained MSSM**: Makes some parameters “quasi-free:”
 - \mathbf{A} and $\mathbf{m}_{\tilde{f}}$ matrices are diagonal (sfermion mixing same as fermion mixing) but otherwise unconstrained; *i.e.*, sfermion-mass unification is not imposed. Authors frequently forget to specify in which basis (mass-diagonal or weak-interaction-diagonal) this constraint is made, leading to much confusion. Frequently, they take only A_t and A_b nonzero since these dominate the sfermion-mass effects.
 - Higgs-sfermion-mass unification not required (as is necessary if sfermion-mass unification not required.).

- **MSSM:** No constraints, not even gaugino-mass unification.

A general comment that can be made about different frameworks is that, obviously, the more restrictive a framework is, the smaller will be the range of predictions for the WIMP-quark and WIMP-gluon scattering cross sections. As noted above, the most restrictive frameworks can be viewed as too restrictive, and possibly even in contradiction with experiment. However, an overly loose framework can make it artificially appear that a large fraction of SUSY WIMP models can never be detected. Where to draw the line is a judgment call.

Appendix B

Noise and Optimal Filtering

B.1 Introduction

The formalism of optimal filtering has traditionally been handed down via oral tradition, with each generation rediscovering truths lost in the shrouded mists of the past through careful study of the ancient writings of Bernard Sadoulet and various others, coupled with deep thought, usually under duress. This appendix is an effort to present some of the basic results of optimal filtering in a pedagogical manner, with care taken to get all the factors of 2 and π correct. I also make the correspondence between the continuous case and the discrete case.

Many of the manipulations performed below (non-convergent integrals, exchanging order of integrations for ill-defined integrals, treating delta functions like functions, etc.) are not rigorously justified. All calculations can always be carried over to the discrete case, where such problems vanish, to check that the results are correct.

B.2 Preliminaries: Fourier Transform and Power Spectral Density Conventions

B.2.1 Fourier Transforms — Continuous Case

First, I define the conventions I use for Fourier transforms. The transform pair $g(t)$ and $\tilde{g}(f)$ are defined by the forward and reverse transforms

$$\begin{aligned}\tilde{g}(f) &= \int_{-\infty}^{\infty} dt g(t) e^{-j\omega t} \\ g(t) &= \int_{-\infty}^{\infty} df \tilde{g}(f) e^{j\omega t}\end{aligned}$$

where $\omega \equiv 2\pi f$ is used for convenience. This sign convention for the argument of the exponential is used so one can make the correspondence $\frac{d}{dt} \leftrightarrow j\omega$, which is expected both from electrical circuit analysis and quantum mechanics. Some confusion may arise about the placement of the 2π ; here, by choosing df as the measure for the frequency integral, the 2π is placed in the denominator of the right side of the reverse transform: $df = \frac{d\omega}{2\pi}$. This choice is made because it makes sense in terms of units: if $g(t)$ carries some physical units (*e.g.*, volts), then $\tilde{g}(f)$ carries units of 1/Hz times that

physical unit (*e.g.*, volts/Hz) because the measure for the integrand is df ; using $d\omega$ would give \tilde{g} units of volts/(radians/sec)). Some authors (*e.g.*, the *CRC Standard Mathematical Tables*) use a symmetric convention (where each transform gets a $\frac{1}{\sqrt{2\pi}}$); this would confound the units.

For the above reasons, it is important to remember that f is the argument of the transform \tilde{g} , not ω . There are many reasons to think otherwise. First, ω is what one thinks of as the conjugate variable to t because these two appear in the exponential. Second, using ω saves writing many 2π 's, especially when solving linear differential equations by transforming to frequency space. Or, it may just appear that ω is the natural variable; for example, when $g(t) = e^{-t/\tau}$, then $\tilde{g}(f) = \tau/(1 + 2\pi j f \tau)$, but one is tempted to write $\tilde{g}(\omega) = \tau/(1 + j\omega\tau)$. Another reason is that, in actually calculating some of these integrals, one does a contour integral in the complex ω plane, not the f plane. Despite all these reasons to use ω , it is misleading to make ω the argument of the function \tilde{g} because this implies that the correct measure for integration of \tilde{g} is $d\omega$; however, one finds that one always has to use $d\omega/2\pi$, and thus the true measure for the function is df .

A number of useful properties make later manipulations and calculations easier. First, it is easy to show

$$\begin{aligned} g(-t) &\xleftrightarrow{\mathcal{FT}} \tilde{g}^*(f) \\ g(t) \text{ real} &\iff \tilde{g}(-f) = \tilde{g}^*(f) \end{aligned}$$

The δ -functions are defined by

$$\begin{aligned} \delta(f) &= \int_{-\infty}^{\infty} dt e^{-j\omega t} = 2\pi\delta(\omega) \\ \delta(t) &= \int_{-\infty}^{\infty} df e^{j\omega t} = \int_{-\infty}^{\infty} \frac{d\omega}{2\pi} e^{j\omega t} \end{aligned}$$

It is important to be careful with the factors of 2π .

A very useful result is the *convolution theorem*:

$$\tilde{g}(f)\tilde{h}(f) \xleftrightarrow{\mathcal{FT}} [g * h](t) \equiv \int_{-\infty}^{\infty} dt_1 g(t_1) h(t - t_1)$$

where $[g * h](t)$ signifies the convolution of g and h . Note the sign of the argument of h . Note also the strange units of the convolution: if g and h are in volts, the convolution carries volts² sec, or volts²/Hz. This is rectified in the discrete case. The convolution of g and h at time t corresponds to the following sequence of operations: time reverse h ; shift the time-reversed h later in time (to the right) by t ; multiply the time-reversed, shifted h against g ; and integrate this product. It is instructive to prove the convolution theorem explicitly because it illustrates one place where it is important to keep track of factors of 2π :

$$\begin{aligned} \mathcal{FT}\{[g * h](t)\} &= \int_{-\infty}^{\infty} dt e^{-j\omega t} \int_{-\infty}^{\infty} dt_1 g(t_1) h(t - t_1) \\ &= \int_{-\infty}^{\infty} dt e^{-j\omega t} \int_{-\infty}^{\infty} dt_1 \int_{-\infty}^{\infty} df_1 \tilde{g}(f_1) e^{j\omega_1 t_1} \int_{-\infty}^{\infty} df_2 \tilde{h}(f_2) e^{j\omega_2 (t - t_1)} \\ &= \int_{-\infty}^{\infty} dt e^{-j\omega t} \int_{-\infty}^{\infty} df_1 \tilde{g}(f_1) \int_{-\infty}^{\infty} df_2 \tilde{h}(f_2) e^{j\omega_2 t} \int_{-\infty}^{\infty} dt_1 e^{j(\omega_1 - \omega_2)t_1} \end{aligned}$$

where $g(t_1)$ and $h(t - t_1)$ are expanded in terms of their transforms and integration order is exchanged. It holds that $\int_{-\infty}^{\infty} dt_1 e^{j(\omega_1 - \omega_2)t_1} = 2\pi\delta(\omega_1 - \omega_2) = \delta(f_1 - f_2)$. Therefore,

$$\begin{aligned}\mathcal{FT}\{[g * h](t)\} &= \int_{-\infty}^{\infty} dt e^{-j\omega t} \int_{-\infty}^{\infty} df_1 \tilde{g}(f_1) \int_{-\infty}^{\infty} df_2 \tilde{h}(f_2) e^{j\omega_2 t} \delta(f_1 - f_2) \\ &= \int_{-\infty}^{\infty} dt e^{-j\omega t} \int_{-\infty}^{\infty} df_1 \tilde{g}(f_1) \tilde{h}(f_1) e^{j\omega_1 t}\end{aligned}$$

Interchanging the order of integration and using $\int_{-\infty}^{\infty} dt e^{j(\omega_1 - \omega)t} = \delta(f_1 - f)$ again yields

$$\mathcal{FT}\{[g * h](t)\} = \tilde{g}(f) \tilde{h}(f)$$

The convolution has the property (provable by changing variables from t_1 to $t_2 = t - t_1$)

$$[g * h](t) = [h * g](t)$$

The convolution theorem is very useful for linear systems, such as filters: typically, the effect of a linear system is easily represented in Fourier space as multiplication by a transfer function. The convolution theorem thus relates the filter's transfer function in Fourier space to its effect in time. By using a δ -function for g , the convolution theorem implies that the transform of the transfer function is just the impulse response of the system, its response to a δ -function input. One can see intuitively that, for a causal filter (one whose impulse response is zero for negative time), the convolution of the signal g with the impulse response h calculates the output at time t by summing up the impulse responses of the filter to the input over earlier times.

A corollary of the convolution theorem is

$$\begin{aligned}\tilde{g}^*(f) \tilde{h}(f) &\xleftrightarrow{\mathcal{FT}} [g \otimes h](t) \equiv \int_{-\infty}^{\infty} dt_1 g(t_1) h(t + t_1) \\ &= \int_{-\infty}^{\infty} dt_1 g(t_1 - t) h(t_1)\end{aligned}$$

where $[g \otimes h](t)$ is the cross-correlation of g and h (again, with weird units). I call this the *cross-correlation theorem*, though this is not general practice. The cross-correlation is easy to visualize: in the first form, shift h earlier in time by t , multiply against g , and integrate the product; in the second form, shift g later in time by t , multiply against h , and integrate the product. This corollary is easy to prove by applying the convolution theorem to the time reverse of g ; this gives \tilde{g}^* on the left side and yields the sign change needed to produce the right side of the second line. Note that the cross-correlation, unlike the convolution, is not commutative:

$$[h \otimes g](t) = [g \otimes h](-t)$$

The cross-correlation and convolution can be related by a time reversal:

$$\begin{aligned}[g \otimes h](t) &\xleftrightarrow{\mathcal{FT}} \tilde{g}^*(f) \tilde{h}(f) \\ &= \tilde{g}_r(f) \tilde{h}(f) \\ &\xleftrightarrow{\mathcal{FT}} [g_r * h](t)\end{aligned}$$

where $g_r(t) = g(-t)$ is the time-reverse of g .

Finally, a corollary of the corollary is *Parseval's Theorem*:

$$\int_{-\infty}^{\infty} dt [g(t)]^2 = \int_{-\infty}^{\infty} df |\tilde{g}(f)|^2$$

This can be proven by integrating both sides of the cross-correlation theorem over f :

$$\begin{aligned} \int_{-\infty}^{\infty} df \tilde{g}^*(f) \tilde{g}(f) &= \int_{-\infty}^{\infty} df \int_{-\infty}^{\infty} dt e^{-j\omega t} \int_{-\infty}^{\infty} dt_1 g(t_1) g_1(t + t_1) \\ &= \int_{-\infty}^{\infty} dt_1 g(t_1) \int_{-\infty}^{\infty} dt g(t + t_1) \int_{-\infty}^{\infty} df e^{-j\omega t} \\ &= \int_{-\infty}^{\infty} dt_1 g(t_1) \int_{-\infty}^{\infty} dt g(t + t_1) \delta(t) \\ &= \int_{-\infty}^{\infty} dt_1 g(t_1) g(t_1) \end{aligned}$$

B.2.2 Fourier Transforms — Discrete Case

In reality, signals are not sampled continuously and over infinite time (though sometimes this experiment makes it look like the second statement may hold...). First consider the reduction of the sampling period to a finite time, $2T$. The proper transform pair is now

$$\begin{aligned} \tilde{g}_n &= \frac{1}{2T} \int_{-T}^T dt g(t) e^{-j\omega_n t} \\ g(t) &= \sum_{n=-\infty}^{\infty} \tilde{g}_n e^{j\omega_n t} \end{aligned}$$

with $f_n = \frac{n}{2T}$ and $\omega_n = 2\pi f_n$ as usual. One can justify this retroactively by identifying $df = \frac{1}{2T}$ and realizing the continuous case corresponds to $T \rightarrow \infty$; here, df has been shifted into the forward transform. Another way to check the transforms is to just substitute the first formula into the second one and see that one has an identity (recognizing $\sum_{n=-\infty}^{\infty} e^{j\omega_n t} = 2T\delta(t)$: one needs the $2T$ to yield the correct time units). The use of frequency bins of a given width can be interpreted as a version of the uncertainty principle — by sampling for only a finite time, only a nonzero frequency resolution can be achieved, given by the bin width. Note that the bandwidth is still infinite — there is information up to arbitrarily high frequency because the time signal is continuous. The units are different also: \tilde{g}_n now carries the same units as $g(t)$. One can make the correspondence

$$\tilde{g}(f) \longleftrightarrow \frac{\tilde{g}_n}{df} = 2T \tilde{g}_n$$

This will be useful below to convert from the continuous case to the discrete case.

This intermediate step to discreteness is not useful, so I immediately move to the fully discrete case. The transform pair is defined by

$$\tilde{g}_n = \frac{1}{N} \sum_{k=-\frac{N}{2}}^{\frac{N}{2}-1} g_k e^{-j\omega_n t_k}$$

$$g_k = \sum_{n=-\frac{N}{2}}^{\frac{N}{2}-1} \tilde{g}_n e^{j\omega_n t_k}$$

where $g_k \equiv g(t_k) \equiv g(k\Delta t)$ and $2T = N\Delta t$. That is, dt has been replaced by the sampling interval Δt and has been cancelled everywhere. The frequency binning is the same as for the intermediate case; that is, it is only the limited sampling period that gives a finite frequency resolution. The feature introduced by sampling at finite frequency is reduction of the bandwidth. This is the Nyquist theorem: by sampling at a finite frequency, all information above half the sampling frequency is lost. The information is not actually lost; rather, it is aliased into the frequency range $\frac{N}{2}\frac{1}{2T}, \dots, (\frac{N}{2}-1)\frac{1}{2T}$. (This is easy to show by trying to transform a signal $g_k = e^{j\omega t_k}$ where $f > \frac{N}{2}\frac{1}{2T} = \frac{1}{2\Delta t}$.) The correspondence

$$\tilde{g}(f) \longleftrightarrow \frac{\tilde{g}_n}{df} = 2T \tilde{g}_n$$

continues to hold. The units of g_k are the same as $g(t)$.

The δ -functions take the form

$$\begin{aligned} \delta(f_n) &= \frac{1}{N} \sum_{k=-\frac{N}{2}}^{\frac{N}{2}-1} e^{-j\omega_n t_k} \\ \delta(t_n) &= \frac{1}{N} \sum_{k=-\frac{N}{2}}^{\frac{N}{2}-1} e^{j\omega_k t_n} \end{aligned}$$

Note that these functions now take on the values 0 or 1, rather than 0 or ∞ . The factors of 2π do not appear in the discrete case.

In the discrete case, the convolution and cross-correlation are defined with more sensible units:

$$\begin{aligned} [g * h]_n &= \frac{1}{N} \sum_{m=-\frac{N}{2}}^{\frac{N}{2}-1} g_m h_{n-m} \\ [g \otimes h]_n &= \frac{1}{N} \sum_{m=-\frac{N}{2}}^{\frac{N}{2}-1} g_m h_{n+m} \end{aligned}$$

That is, the cross-correlation and convolution carry units of volts². The $\frac{1}{N}$ factor is applied for two reasons: first, correspondence with the intermediate case gives $\frac{1}{N} \leftrightarrow \frac{\Delta t}{2T}$: this would give a sensible definition for the convolution and cross-correlation in the intermediate case; second, with this normalization, both the convolution and cross-correlation at zero shift give $\langle [g(t)]^2 \rangle$ for $h = g$, which is certainly more reasonable than giving $N\langle [g(t)]^2 \rangle$.

In the discrete case, there is the minor issue of the edges: since the traces do not extend in each direction to ∞ , when one shifts a trace during convolution or cross-correlation, samples are lost off the edge because there is nothing against which to multiply them. One might try

correcting the normalization of $[g * h]_n$ by dividing by $N - |m|$ rather than N . How well this works depends on the traces themselves: if the traces go to zero at the ends of the window, then the “uncorrected” formula is in fact the best estimator of the true value; however, if the traces tend to some nonzero value at the edges of the window, then the “uncorrected” formula is quite a bad estimator. However, in practice, the “corrected” form does not fix this. One might hope that the use of a Hanning window would fix these edge effects; it also does not. The fundamental problem is that, by using traces that end before the pulse, one artificially changes the pulse shape, and thus its Fourier transform, in an unrecoverable way. The information past the edge of the digitization window is lost. In practice, for the pulse-analysis case where the trace and filter both are zero for many samples at the start of the window but are nonzero at the end, the best solution is to slightly shorten the data trace so that, in effect, the filter trace has more samples at its end. In the pretrigger direction, there is no edge effect because both traces are very close to zero. In the posttrigger direction, the longer filter trace eliminates the edge effect as long as the shift value is not larger than the number of extra samples in the filter trace; this typically holds.

With the above definitions, the convolution and cross-correlation theorems hold as before:

$$\begin{aligned}\tilde{g}_n \tilde{h}_n &\xleftrightarrow{\mathcal{FT}} [g * h](t) \\ \tilde{g}_n^* \tilde{h}_n &\xleftrightarrow{\mathcal{FT}} [g \otimes h](t)\end{aligned}$$

Parseval’s theorem is

$$\frac{1}{N} \sum_{k=-\frac{N}{2}}^{\frac{N}{2}-1} g_k^2 = \sum_{n=-\frac{N}{2}}^{\frac{N}{2}-1} |\tilde{g}_n|^2$$

Note the position of the $\frac{1}{N}$.

B.3 Noise

The formalism for noise is confusing at first because the units that noise is usually quoted in, $V/\sqrt{\text{Hz}}$, do not correspond directly to any physical quantity. One becomes so accustomed to the convenience of having noises in $V/\sqrt{\text{Hz}}$ rather than V^2/Hz that one tends to forget the units are nonsensical. In this section, I explain the formalism for noise and why it carries units of $V/\sqrt{\text{Hz}}$.

The fluctuations of a physical voltage are assumed to be a Gaussian-distributed random variable; that is, $v(t)$ is chosen from a Gaussian distribution whose variance is $\langle [v(t)]^2 \rangle$ ($\langle v(t) \rangle = 0$ is assumed for simplicity). However, $\langle [v(t)]^2 \rangle$ does not fully determine the noise characteristics of the system — it does not contain information about correlations of $v(t)$ with itself in time. Physically, it is important to consider such correlations — for example, for a temperature fluctuation at time t , it takes a time τ for the extra energy associated with the fluctuation to flow out of the system, so $T(t)$ contains some information about $T(t + \tau)$. This information is contained in the autocorrelation function $R(\tau)$:

$$\begin{aligned}R(\tau) &= \langle v(t)v(t + \tau) \rangle \\ &= \lim_{T \rightarrow \infty} \frac{1}{2T} [v \otimes v](\tau) \\ &= \lim_{T \rightarrow \infty} \frac{1}{2T} \int_{-T}^T dt v(t) v(\tau + t)\end{aligned}$$

Note that this differs from the definition of the cross-correlation for the continuous case by a factor $2T$; the $2T$ is inserted here to give the autocorrelation function reasonable units. Also, since $v(t)$ extends infinitely into the past and future, the integral is infinite; the $2T$ makes it finite.

Such correlations are also coded in the frequency spectrum of the noise. The Fourier transform of the autocorrelation function is the noise power spectral density, $J(f)$:

$$J(f) = \lim_{T \rightarrow \infty} \int_{-T}^T dt R(t) e^{-j\omega t}$$

which has units of V^2/Hz . One typical case is $R(t) = \sigma^2 e^{-|t|/\tau}$, which holds for linear systems with a single decay time. The resulting power spectral density is $J(f) = 2\tau\sigma^2[1 + (\omega\tau)^2]^{-1}$. The noise PSD rolls off at frequencies above $(2\pi\tau)^{-1}$, expressing the strong autocorrelation of the noise for time separations smaller than τ . Note that all noises must be rolled off at some frequency; otherwise, $J(f)$ does not tend to zero as $f \rightarrow \infty$ and $R(t)$ becomes infinite. Perfect “white noise,” with $J(f)$ a constant, does not exist. However, any noise of the first form can be considered white for $f \ll (2\pi\tau)^{-1}$; this expresses the fact that, for $t \gg \tau$, the autocorrelation function tends to zero: the noise appears uncorrelated in time for $t \gg \tau$.

A corollary of the definition of the power spectral density is

$$R(t) = \int_{-\infty}^{\infty} df J(f) e^{j\omega t}$$

and, specifically,

$$\langle [v(t)]^2 \rangle = R(0) = \int_{-\infty}^{\infty} df J(f)$$

This expression ultimately justifies the use of $J(f)$ to represent the frequency behavior of the noise: the integral of the noise power spectral density gives the noise variance in time. The units of $J(f)$, V^2/Hz , are thus sensible. The quantity usually discussed or given in noise spectra is $\sqrt{J(f)}$, which thus has units of $V/\sqrt{\text{Hz}}$. In many places, this second quantity is incorrectly referred to as the power spectral density (including in earlier sections of this dissertation). Usually, the context or units indicate whether it is $J(f)$ or $\sqrt{J(f)}$ that is implied by “power spectral density.” The above relation can also be used as a check that calculational routines have been coded correctly.

The advantage of moving to frequency space for noise is that, for linear systems, noise components at different frequencies are independent. This results simply from the fact that, for linear systems, the behavior of the system at frequency f is independent of its behavior at other frequencies. Consider, for example, a thermal system with heat capacity C coupled to a thermal bath by a coupling G and at temperature $T = \delta T(t) + T_0$. In time, energy conservation gives

$$C \frac{d\delta T}{dt} = -GP(t)$$

$P(t)$ is just the noise power exchanged between the system and the thermal bath; though the system and bath are at the same DC temperature and there is no net power flow, there is power flowing back and forth to maintain the equilibrium condition. There are correlations in time according to the above equation. However, its transform is

$$j\omega C \widetilde{\delta T}(f) = -G\widetilde{P}(f)$$

where C and G are taken to be independent of frequency. $P(t)$ is the driving force and can be specified in either time or frequency space. The solution for $\widetilde{\delta T}(f)$ is

$$\widetilde{\delta T}(f) = \frac{1}{G} \frac{\widetilde{P}(f)}{1 + j\omega\tau}$$

where $\tau = C/G$ is the thermal time constant. Thus, the behavior of the temperature fluctuations at frequency f depends only on $\widetilde{P}(f)$ and not on $\widetilde{\delta T}(f)$ at other frequencies. Typically, $P(f)$ (or its analogue) can be traced back to a physical process for which there should be no correlations among frequencies, at least for timescales long compared to the timescale of the physical processes involved, which are usually quite short, 10^{-12} s or less. This lack of correlation is very much unlike the behavior of $\delta T(t)$, where there are strong correlations between $\delta T(t)$ and $\delta T(t + \delta t)$ for $|\delta t| \lesssim \tau$. Thus, frequency space is a basis in which the noise is diagonal, which is in general very convenient. It is also important for calculating a properly normalized χ^2 when fitting a pulse-shape model to data.

Although the noise power spectral density can be determined from the autocorrelation function calculated from many noise traces (traces that have no events in them), it is common practice to calculate it directly from the Fourier transform of the noise traces. This can be seen as follows:

$$\begin{aligned} J(f) &= \lim_{T \rightarrow \infty} \int_{-T}^T dt R(t) e^{-j\omega t} \\ &= \lim_{T \rightarrow \infty} \int_{-T}^T dt e^{-j\omega t} \lim_{T \rightarrow \infty} \frac{1}{2T} [v \otimes v](t) \\ &= \lim_{T \rightarrow \infty} \int_{-T}^T dt e^{-j\omega t} \lim_{T \rightarrow \infty} \frac{1}{2T} \int_{-\infty}^{\infty} df_1 e^{j\omega_1 t} \widetilde{v}^*(f_1) \widetilde{v}(f_1) \\ &= \lim_{T \rightarrow \infty} \frac{1}{2T} \int_{-\infty}^{\infty} df_1 e^{j\omega_1 t} |\widetilde{v}(f_1)|^2 \delta(f - f_1) \\ &= \lim_{T \rightarrow \infty} \frac{1}{2T} |\widetilde{v}(f)|^2 \end{aligned}$$

where limit and integration orders have been freely exchanged and the definition of $\delta(f)$ has been used. That is, the power spectral density is just the squared amplitude of the Fourier transform divided by the sampling period.

It is necessary to convert the above relations to the discrete case for application. The autocorrelation function is

$$\begin{aligned} R(t_n) = R_n &= [v \otimes v]_n \\ &= \frac{1}{N} \sum_{m=-\frac{N}{2}}^{\frac{N}{2}-1} v_m v_{n+m} \end{aligned}$$

where the $2T$ denominator is no longer needed because the cross-correlation includes it for the discrete case. The $\frac{1}{N}$ factor plays the normalizing role of $\frac{1}{2T}$. The power spectral density can be written in two forms:

$$J_p = J(f_p) = \mathcal{FT}[R(t_k)]$$

$$= \frac{1}{N} \sum_{k=-\frac{N}{2}}^{\frac{N}{2}-1} e^{-j\omega_k t_n} \sum_{m=-\frac{N}{2}}^{\frac{N}{2}-1} v_m v_{n+m}$$

corresponds to the definition of $J(f)$ in terms of the autocorrelation function. The more useful form is

$$\begin{aligned} J(f_p) &= \lim_{T \rightarrow \infty} \frac{1}{2T} |\tilde{v}(f_p)|^2 \\ &= \lim_{T \rightarrow \infty} \frac{1}{2T} |2T \tilde{v}_p|^2 \\ &= 2T |\tilde{v}_p|^2 \end{aligned}$$

where the limit has been discarded in the discrete case. This is the form that is usually used for calculating $J(f)$: a number of noise traces are acquired, $|\tilde{v}_p|^2$ calculated for each trace, and the mean value of $|\tilde{v}_p|^2$ calculated, multiplying by $2T$. This final expression is what one would expect: the \tilde{v}_p are in units of volts and $\frac{1}{2T}$ is the frequency bin width, so the expression gives V^2/Hz .

It is also important to understand the relation between an individual noise realization $v(t)$ (or $\tilde{v}(f)$) and $J(f)$. $J_p/(2T)$ gives the mean square absolute value of the frequency component \tilde{v}_p . Under the assumption of Gaussianity, $J_p/(2T)$ thus gives the variance of the Gaussian distribution from which \tilde{v}_p is drawn. Since \tilde{v}_p is complex, $J_p/(2T)$ only specifies the distribution for $|\tilde{v}_p|$. However, again because of linearity, the real and imaginary components of \tilde{v}_p are independent. One can choose one of two prescriptions. One is to pick $\Re[\tilde{v}_p]$ and $\Im[\tilde{v}_p]$ independently from a Gaussian distribution of variance $(J_p/2)/(2T)$; then $\langle |\tilde{v}_p|^2 \rangle = J_p/(2T)$. The other is to pick $|\tilde{v}_p|$ from a Gaussian of variance $J_p/(2T)$, rectifying negative values, and to pick the phase of \tilde{v}_p from a uniform distribution over the interval $[0, 2\pi)$. Finally, for most applications, $v(t)$ is real, and thus $\tilde{v}(-f_p) = \tilde{v}^*(f_p)$: the negative frequency components are not independent of the positive ones.

B.4 Optimal Pulse-Height and Time-Offset Estimators

With the above formalism, the problem of finding optimal pulse-height and time-offset estimators for a pulse can be formulated rigorously. The procedure described here is termed “optimal filtering” for reasons that will become apparent. A real pulse has the form

$$v(t) = As(t) + n(t)$$

where $s(t)$ is the expected pulse shape (normalized to have peak height of 1), A is the amplitude to be estimated, and $n(t)$ is a particular noise realization. Let the noise power spectral density be given by $J(f)$. It is desired to find the best estimator for A . To pose the question clearly, one needs a criterion for “best.” This is defined by the χ^2 of the fit of the event to the expected pulse shape:

$$\chi^2 = \int_{-\infty}^{\infty} df \frac{|\tilde{v}(f) - A\tilde{s}(f)|^2}{J(f)}$$

As justified above, the χ^2 is calculated in frequency space because different frequency components are independent. The above χ^2 is properly normalized because

$$df \frac{\langle |\tilde{v}(f) - A\tilde{s}(f)|^2 \rangle}{J(f)} = df \frac{\langle |\tilde{n}(f)|^2 \rangle}{J(f)}$$

$$\begin{aligned}
&= df \lim_{T \rightarrow \infty} 2T \\
&= 1
\end{aligned}$$

That is, $\langle \chi^2 \rangle$ equals the sum of the number of frequency components, which is the number of degrees of freedom and is formally infinite. It becomes finite in the discrete case. Note that though the negative frequency components are not independent of the positive ones, the positive components each have two degrees of freedom, amplitude and phase, or real and imaginary components, so the χ^2 is indeed properly normalized. It is straightforward to find the best estimator \hat{A} by minimizing χ^2 with respect to A :

$$\hat{A} = \frac{\int_{-\infty}^{\infty} df \frac{\tilde{s}^*(f) \tilde{v}(f)}{J(f)}}{\int_{-\infty}^{\infty} df \frac{|\tilde{s}(f)|^2}{J(f)}}$$

One can show that this estimator is unbiased; *i.e.*, $\langle \hat{A} \rangle = A$. It is interesting to calculate the expected variance of A , $\sigma_A^2 = \langle [\hat{A} - A]^2 \rangle$, which gives the expected resolution. It is an interesting exercise in Fourier algebra to do this directly by calculating $\langle [\hat{A}]^2 \rangle$ and using $\langle [\hat{A} - A]^2 \rangle = \langle [\hat{A}]^2 \rangle - A^2$; one has to take special care with the correlation between $n(f)$ and $n(-f)$. However, in the interest of saving space, I use the general result $\sigma_A^2 = \left[\frac{1}{2} \frac{\partial^2 \chi^2}{\partial A^2} \right]^{-1}$, which yields

$$\sigma_A^2 = \left[\int_{-\infty}^{\infty} df \frac{|s(f)|^2}{J(f)} \right]^{-1} \quad (\text{B.1})$$

This last formula is extremely useful. It indicates the best possible resolution achievable given the assumed pulse shape and noise power spectral density, so it can be used to gauge whether the fitting procedure is meeting its expected performance. In theoretical comparisons of different types of particle-detection schemes, the above formula can be used to estimate the optimal performance of each scheme.

The above formalism can be extended to fit for an arbitrary time offset. As described in Chapter 6, such a time-offset search is necessary in cases where the pulse is not in the expected position in the digitizer window. A time-offset search is performed to find an ionization pulse in the digitized trace for phonon-trigger events. More generally, it is used to correct for variation with pulse amplitude of the position of the pulse relative to the trigger time, though the search range is much shorter in the latter case. The χ^2 is defined as before, but this time allowing for a time offset:

$$\chi^2 = \int_{-\infty}^{\infty} df \frac{|\tilde{v}(f) - A e^{-j\omega t_0} \tilde{s}(f)|^2}{J(f)}$$

If the template pulse normally starts at $t = 0$, the shifted pulse $e^{-j\omega t_0} \tilde{s}(f)$ starts at time $t = t_0$. Minimizing χ^2 with respect to t_0 does not yield a simple formula for \hat{t}_0 because of the more complex dependence of χ^2 on t_0 . Minimizing χ^2 yields

$$\begin{aligned}
- \int_{-\infty}^{\infty} df \frac{\tilde{v}^*(f) A e^{-j\omega t_0} \tilde{s}(f) + \tilde{v}(f) A e^{j\omega t_0} \tilde{s}^*(f)}{J(f)} \Big|_{t_0=\hat{t}_0} &= 0 \\
- 2 \int_{-\infty}^{\infty} df \frac{\tilde{v}^*(f) A e^{-j\omega t_0} \tilde{s}(f)}{J(f)} \Big|_{t_0=\hat{t}_0} &=
\end{aligned}$$

where \hat{t}_0 is the value of t_0 that yields the minimization condition. The two quadratic terms vanish because they are independent of t_0 . The second line is derived by using the relation

$$\int_{-\infty}^{\infty} df \frac{\tilde{v}(f) A e^{j\omega t_0} \tilde{s}^*(f)}{J(f)} = \int_{-\infty}^{\infty} df \frac{\tilde{v}^*(f) A e^{-j\omega t_0} \tilde{s}(f)}{J(f)}$$

which can be demonstrated using the convolution theorem and the fact that $\mathcal{FT}[\tilde{v}(f)]$ and $\mathcal{FT}[e^{-j\omega t_0} \tilde{s}(f)/J(f)]$ are real. The minimization condition can be written in a more illustrative form. Define the *optimal filter* by

$$\tilde{\phi}(f) = \frac{\tilde{s}^*(f)}{J(f)}$$

with Fourier transform $\phi(t)$. $\tilde{\phi}(f)$ does not have the correct units, but this is rectified later. The minimization condition is then (dropping the -2 and the constant A):

$$\left. \frac{\partial}{\partial t_0} [\phi * v](t_0) \right|_{t_0=\hat{t}_0} = 0$$

The prescription is thus to apply the filter $\phi(t)$ to the trace and find the time of the peak. The best estimator for the amplitude can be determined as before, treating $e^{-j\omega \hat{t}_0} \tilde{s}(f)$ as $\tilde{s}(f)$ was treated before; effectively, $e^{-j\omega \hat{t}_0} \tilde{s}(f)$ gives the correct expected pulse shape because it incorporates the time offset. Thus the best estimator for the amplitude is given by

$$\hat{A} = \frac{\int_{-\infty}^{\infty} df \frac{e^{j\omega \hat{t}_0} \tilde{s}^*(f) \tilde{v}(f)}{J(f)}}{\int_{-\infty}^{\infty} df \frac{|\tilde{s}(f)|^2}{J(f)}} \quad (\text{B.2})$$

The numerator is again the convolution of the trace $v(t)$ with the optimal filter $\phi(t)$, evaluated at the time offset \hat{t}_0 . Since \hat{t}_0 corresponds to the time of the peak of the filtered trace, \hat{A} is just proportional to the peak amplitude of the filtered trace. Hence, the procedure is called “optimal filtering.” The denominator is the peak amplitude of the trace given by optimally filtering the expected pulse shape $s(t)$ (with peak amplitude 1); it is a normalization factor that corrects for the fact that the optimal filter changes the peak amplitude. It also rectifies the issue with the units of $\tilde{\phi}(f)$. The expected energy resolution, σ_A^2 is unchanged since it is determined from the second quadratic term in χ^2 and thus is independent of the time offset. However, in the language of filters, it can be seen to have a more intuitive meaning by rewriting:

$$\sigma_A^2 = \frac{\int_{-\infty}^{\infty} df J(f) \left| \frac{\tilde{s}(f)}{J(f)} \right|^2}{\left[\int_{-\infty}^{\infty} df \frac{|\tilde{s}(f)|^2}{J(f)} \right]^2} \quad (\text{B.3})$$

The numerator is the variance in time of the filtered trace: $J(f) |\tilde{s}(f)/J(f)|^2$ is the filtered power spectral density. The denominator is the square of the peak amplitude of the trace given by filtering the expected pulse shape (whose peak height is 1) with the optimal filter. The expression is thus the squared noise-to-signal ratio, $(N/S)^2$, of the filtered expected pulse shape. It is instructive to

write the signal-to-noise ratio explicitly for a pulse of amplitude A :

$$\frac{\hat{A}}{\sigma_A} = \frac{\int_{-\infty}^{\infty} df \frac{e^{j\omega \hat{t}_0} \tilde{s}^*(f) \tilde{v}(f)}{J(f)}}{\left[\int_{-\infty}^{\infty} df J(f) \left| \frac{\tilde{s}(f)}{J(f)} \right|^2 \right]^{1/2}} \quad (\text{B.4})$$

That is, the signal-to-noise ratio is just the ratio of the peak height of the filtered pulse to the filtered noise in time.

Viewed as an impulse response function, the optimal filter is always acausal since it is the time reverse of $\mathcal{FT}[\tilde{s}(f)/J(f)]$, which is causal because $s(t)$ is causal and $J(f)$ is real. In practice, this means optimal filtering cannot be implemented in hardware: to construct the optimally filtered pulse at a given time, one has to know the value of the incoming pulse in the future!

In the case that the noise is white, the formulae become more intuitive. If the noise is white, the optimal filter is just $\tilde{\phi}(f) = \tilde{s}^*(f)$, which yields $\phi(t) = s(-t)$. Since $g_r * h = g \otimes h$ where $g_r(t) = g(-t)$, optimal filtering corresponds to cross-correlating the pulse with the expected shape. The best time offset is given by the time offset that maximizes the cross-correlation, as one would expect.

The expected time resolution can also be calculated using the second derivative of the χ^2 ; in fact, this is the only way to calculate it, given that there is no explicit form for \hat{t}_0 . This yields

$$\sigma_{t_0}^2 = \left[A^2 \int_{-\infty}^{\infty} df \omega^2 \frac{|s(f)|^2}{J(f)} \right]^{-1} \quad (\text{B.5})$$

As one might expect, an additional frequency-weighting factor enters, expressing the fact that time-offset estimation requires more high-frequency information than amplitude estimation. The time resolution decreases as $1/A$: the more energetic the pulse is, the better the time estimation, which is also reasonable.

Finally, it is useful to convert the above formulae to the discrete case. The correspondence is made using

$$\begin{aligned} \tilde{s}^*(f) &\longleftrightarrow \frac{\tilde{s}_n^*}{\Delta f} \\ \tilde{v}(f) &\longleftrightarrow \frac{v_n}{\Delta f} \\ J(f) &\longleftrightarrow J(f_n) \\ \int_{-\infty}^{\infty} df &\longleftrightarrow \sum_{n=-\frac{N}{2}}^{\frac{N}{2}-1} \Delta f \end{aligned}$$

which yields

$$\begin{aligned} \hat{A} &= \frac{\sum_{n=-\frac{N}{2}}^{\frac{N}{2}-1} \Delta f e^{j\omega_n \hat{t}_0} \frac{\tilde{s}_n^*}{\Delta f} \frac{v_n}{\Delta f} \frac{1}{J(f_n)}}{\sum_{n=-\frac{N}{2}}^{\frac{N}{2}-1} \Delta f \frac{|\tilde{s}_n|^2}{[\Delta f]^2} \frac{1}{J(f_n)}} \\ &= \frac{\sum_{n=-\frac{N}{2}}^{\frac{N}{2}-1} e^{j\omega_n \hat{t}_0} \frac{\tilde{s}_n^* v_n}{J(f_n)}}{\sum_{n=-\frac{N}{2}}^{\frac{N}{2}-1} \frac{|\tilde{s}_n|^2}{J(f_n)}} \end{aligned}$$

and

$$\begin{aligned}\sigma_A^2 &= \left[\sum_{n=-\frac{N}{2}}^{\frac{N}{2}-1} \Delta f \frac{|\tilde{s}_n|^2}{[\Delta f]^2} \frac{1}{J(f_n)} \right]^{-1} \\ &= \left[2T \sum_{n=-\frac{N}{2}}^{\frac{N}{2}-1} \frac{|\tilde{s}_n|^2}{J(f_n)} \right]^{-1}\end{aligned}$$

Note the factor of $2T$: this arises because $J(f_n)$ is in V^2/Hz .

B.5 Non-Optimal Pulse-Height Estimation

As mentioned above, optimal filtering cannot be implemented in an analog circuit in hardware. Therefore, it is of interest to determine the expected resolution expression for causal filters. An amplitude estimator can be calculated by analogy to the optimal filter case, giving, for a non-optimal filter $\tilde{g}(f)$:

$$\hat{A} = \frac{\int_{-\infty}^{\infty} df e^{j\omega(\hat{t}_0+t^*)} \tilde{g}(f) \tilde{v}(f)}{\int_{-\infty}^{\infty} df e^{j\omega t^*} \tilde{g}(f) \tilde{s}(f)} \quad (\text{B.6})$$

where the optimal filter $\tilde{s}^*(f)/J(f)$ has been replaced by the non-optimal filter $\tilde{g}(f)$. The extra exponential factor $e^{j\omega t^*}$ requires some explanation. The denominator of the optimal-filter expression, Equation B.2, is the peak of the trace given by filtering the expected pulse shape $s(t)$ with the optimal filter. Effectively, this is a correction factor for the fact that filtering changes the pulse amplitude. When filtering the expected shape by the optimal filter, the peak automatically occurs at zero time offset because the optimal filter and expected pulse shape are already aligned in time. This does not necessarily hold for the non-optimal filter, so the peak has to be found empirically. Furthermore, the time offset of the peak, t^* , must be used to correct the offset found for the data trace: even a pulse with $t_0 = 0$ has its filtered peak offset to t^* . One can show that the above estimator is also unbiased.

The expected energy resolution of the non-optimal filter must be calculated from $\sigma_A^2 = \langle [\hat{A}]^2 \rangle - A^2$ since $\tilde{g}(f)$ does not minimize χ^2 . Again, this is an exercise in Fourier transform algebra that I do not perform explicitly; the result is

$$\sigma_A^2 = \frac{\int_{-\infty}^{\infty} df J(f) |\tilde{g}(f)|^2}{\left[\int_{-\infty}^{\infty} df e^{j\omega t^*} \tilde{g}(f) \tilde{s}(f) \right]^2} \quad (\text{B.7})$$

One can easily see that this reduces to the optimal-filter expression, Equation B.1, in the case $\tilde{g}(f) = \tilde{s}^*(f)/J(f)$ and $t^* = 0$. Furthermore, the expression is analogous to the alternate expression for the optimal-filter energy resolution given by Equation B.3. The numerator is the variance in time of the noise after filtering: $J(f) |\tilde{g}(f)|^2$ is the filtered noise power spectral density. The denominator is the square of the peak amplitude of the trace given by filtering the expected shape $s(t)$ by the non-optimal filter, which is a normalizing factor of the type seen in Equation B.3. The

signal-to-noise ratio for a pulse of amplitude A in the non-optimal-filtering case is

$$\frac{\hat{A}}{\sigma_A} = \frac{\int_{-\infty}^{\infty} df e^{j\omega(\hat{t}_0+t^*)} \tilde{g}(f) \tilde{v}(f)}{\left[\int_{-\infty}^{\infty} df J(f) |\tilde{g}(f)|^2 \right]^{-1/2}} \quad (\text{B.8})$$

As with the optimal-filter case, Equation B.4, the signal-to-noise ratio is just the ratio of the peak height of the filtered pulse to the filtered noise in time.

To illustrate the non-optimal case further, consider the simplest possible non-optimal filter: no filtering, $\tilde{g}(f) = 1$. The pulse-height estimator is just the peak amplitude of the unfiltered pulse because the denominator of Equation B.6 reduces to 1 and the numerator is just the pulse itself. The energy resolution expression, Equation B.7, also reduces: the denominator is 1 and the numerator is $\langle [v(t)]^2 \rangle = \int_{-\infty}^{\infty} df J(f)$. Since one uses the peak of the unfiltered pulse as the estimator, the noise in time gives the resolution directly.

The expressions in the discrete case for the non-optimal amplitude estimator and resolution are

$$\begin{aligned} \hat{A} &= \frac{\sum_{n=-\frac{N}{2}}^{\frac{N}{2}-1} e^{j\omega_n \hat{t}_0} \tilde{g}_n \tilde{v}_n}{\sum_{n=-\frac{N}{2}}^{\frac{N}{2}-1} \tilde{g}_n \tilde{s}_n} \\ \sigma_A^2 &= \frac{1}{2T} \frac{\sum_{k=-\frac{N}{2}}^{\frac{N}{2}-1} J(f_n) |\tilde{g}_n|^2}{\left[\sum_{k=-\frac{N}{2}}^{\frac{N}{2}-1} e^{j\omega t^*} \tilde{g}_n \tilde{s}_n \right]^2} \end{aligned}$$

B.6 Applications

The obvious application of the optimal-filtering formalism is to optimally fit the energy of acquired pulses. Optimal filtering can be implemented fully on digitized traces of sufficient length. For Run 19, optimal filtering was particularly necessary because of the large amount of 1-kHz cross-talk — optimal filtering notches out the frequencies with large cross-talk, leaving the resolution essentially unchanged from the case in which there is no cross-talk. Optimal filtering is implemented in a fairly straightforward way. The trace is Fourier transformed and filtered by the optimal filter, which is calculated from noise traces and the pulse template. The filtered pulse is transformed back to time. The time offset and amplitude are given by the time offset of the peak and the peak amplitude. Other aspects of the implementation are discussed in Chapter 6.

An important application of both the amplitude resolution expression, Equation B.1, and the time resolution expression, Equation B.5, is to determine the maximum digitization frequency needed. The ionization pulses can be modelled approximately as 2-pole exponentials, with one pole at the fall time, τ_f , and a second at the rise time, τ_r , with

$$s(f) = \frac{\tau_f}{1 + j\omega\tau_f} \frac{\tau_r}{1 + j\omega\tau_r}$$

$s(f)$ is flat up to $(2\pi\tau_f)^{-1}$, falls as $1/f$ between $(2\pi\tau_f)^{-1}$ and $(2\pi\tau_r)^{-1}$, and falls as $1/f^2$ above $(2\pi\tau_r)^{-1}$. Assuming white noise, which is not a bad approximation for the ionization channels,

Channel	BLIP3	BLIP4	BLIP5	BLIP6
Optimal Filter				
QI [μV]	10	11	12	12
QO [μV]	10	13	15	17
P1 [nV]	23	32	32	32
P2 [nV]	22	32	32	34
Non-Optimal Filter				
QI [μV]	24	22	28	25
QO [μV]	28	31	33	37
P1 [nV]	64	76	61	73
P2 [nV]	60	79	65	111

Table B.1: Resolutions for optimal and non-optimal filtering for Run 19 ionization and phonon channels. Resolutions are in pulse height at the first-stage ionization amplifier output and the phonon amplifier input. These are *calculated*, not measured, values.

the interesting quantity, $|s(f)|^2/J(f)$, is flat, falls as $1/f^2$, and falls as $1/f^4$ in the three regimes. Thus, the integral of $\frac{|s(f)|^2}{J(f)}$ up to a frequency f_c , which is the denominator of the amplitude resolution formula, Equation B.1, is linear in f_c up to $(2\pi\tau_f)^{-1}$, goes as $1/f_c$ between $(2\pi\tau_f)^{-1}$ and $(2\pi\tau_r)^{-1}$, and as $1/f_c^3$ above $(2\pi\tau_r)^{-1}$. Since τ_f and τ_r are typically separated by about an order of magnitude, little improvement in energy resolution is gained above $(2\pi\tau_f)^{-1}$. For the time resolution, two additional powers of frequency enter, so the scalings are as f_c^2 , f_c^0 , and $1/f_c$ in the three regimes. Little improvement in time resolution is gained above $(2\pi\tau_r)^{-1}$. As is described below, this result only holds for fitting to an analytic form; it is modified for template fitting.

The main application of non-optimal filtering is to find the optimal filters for the trigger circuitry. The filter that gives the best resolution also gives the lowest energy threshold because it maximizes the signal-to-noise ratio. The resolution expression, Equation B.7, can be used to compare different types of filters and to optimize the parameters of a given type of filter. The RTF trigger circuits use 1-pole low-pass and high-pass filters whose time constants have been optimized using Equation B.7. It is interesting to compare the expected optimal and non-optimal resolutions to see how much worse the resolution is for this particular non-optimal filter. This is done in Table B.1 for the Run 19 ionization and phonon channels. In general, the non-optimally filtered resolutions are a factor of 2 to 3 worse than the optimally filtered resolutions.

B.7 Real-World Effects

B.7.1 Sampling Period

If there are sharp features in the noise spectrum, such as 1-kHz cross-talk, it is important to use a long sampling period, $2T$, so that the frequency bin width, $\frac{1}{2T}$, is very small compared to the total bandwidth. This allows the bins containing spectral features to be discarded with negligible loss of signal-to-noise. For Run 19, very long ionization traces, 12.8 ms, were taken, yielding $\Delta f = 78.125$ Hz. The fall time of the ionization pulses is about 40 μs , corresponding to

about 4 kHz, so less than 10% of the bandwidth useful for energy estimation was lost by discarding the 1, 2, 3, and 4 kHz bins.

B.7.2 Expected Amplitude Distribution for Fit with Time Search

The amplitude resolution given by Equation B.1 is only valid if the time offset is not strongly correlated with the amplitude estimate. This holds if the pulse is of sufficient amplitude that the time offset is well established, independent of fluctuations around the expected amplitude; recall that the time-offset resolution decreases as $1/A$. However, near threshold or for noise traces, the time offset and amplitude are strongly correlated. An expression for the expected distribution of fitted amplitudes can be calculated in this case. The following argument was first suggested to me by Rick Gaitskell.

The case of a pulse well above threshold can be mimicked for noise traces by fixing the time offset and calculating the amplitude estimator in the standard way. The expected distribution of amplitudes is Gaussian with width σ_V , as calculated by optimal or non-optimal filtering. That is,

$$P(V) = \frac{1}{\sigma_V \sqrt{2\pi}} \exp\left(-\frac{V^2}{2\sigma_V^2}\right)$$

The Gaussianity of the distribution is corroborated by the baseline resolution distributions shown in Chapter 4.

Now, let t_0 be a free parameter that can take values over a range $M\Delta t$, where Δt is the sampling interval. M indicates the width of the search window in samples. Also, assume that the values of t_0 are restricted so the pulse does not approach the edges of the digitized trace; *i.e.*, no edge effects occur. Each value of t_0 yields a value $V(t_0)$ drawn from the above Gaussian distribution. The optimal-filter prescription is to take the largest such value of V as the best pulse-height estimator. The value of t_0 yielding this value of V is the best time estimator. Thus, the largest V , V_{max} , out of a sample of M values of V drawn from the above distribution is taken. The probability of this procedure giving a value V_{max} is given by the probability that there is value of t_0 giving $V = V_{max}$ and that the other $M - 1$ samples give $V < V_{max}$. There are M ways for this to happen since any of the M samples may take the value V_{max} . Thus, the distribution for V_{max} is

$$\begin{aligned} P(V_{max}) &= M \left[\int_{-\infty}^{V_{max}} dV P(V) \right]^{M-1} P(V_{max}) \\ &= M [\text{erf}(V_{max}, \sigma_V)]^{M-1} \frac{1}{\sigma_V \sqrt{2\pi}} \exp\left(-\frac{V_{max}^2}{2\sigma_V^2}\right) \end{aligned}$$

B.7.3 Jitter

As shown above, for a 2-pole exponential pulse, the bulk of the signal-to-noise for the t_0 estimation comes from frequencies below $(2\pi\tau_r)^{-1}$. Therefore, in principle, it is unnecessary to digitize with a Nyquist frequency larger than $(2\pi\tau_r)^{-1}$. However, this result only holds in the case that the pulses are fit to an analytic form that can be calculated for time shifts that are not integral values of the sample interval Δt . If one is performing a template fit, the template can only be shifted by integral multiples of Δt . Essentially, the convolution of the optimal filter with

the pulse cannot be calculated between time bins. This degrades both the time and amplitude estimation; the phenomenon is a form of time jitter. The time shift can only be calculated to a precision of Δt . The effect on the amplitude is slightly more subtle: since the peak of the convolution gives the amplitude estimation, and one does not have the convolution for non-integral time values, the peak of the convolution is underestimated when one takes the largest of the two values that bracket the peak. The expected underestimation of the amplitude is

$$\begin{aligned}
 \delta E(\delta t) &= E(0) - E(\delta t) \\
 &= E(0) \frac{\sum_{k=-\frac{N}{2}}^{\frac{N}{2}-1} \frac{|\bar{s}_k|^2}{J_k} [1 - e^{j\omega_k \delta t}]}{\sum_{k=-\frac{N}{2}}^{\frac{N}{2}-1} \frac{|\bar{s}_k|^2}{J_k}} \\
 &= E(0) \frac{\sum_{k=-\frac{N}{2}}^{\frac{N}{2}-1} \frac{|\bar{s}_k|^2}{J_k} [1 - \cos(2\pi f_k \delta t)]}{\sum_{k=-\frac{N}{2}}^{\frac{N}{2}-1} \frac{|\bar{s}_k|^2}{J_k}}
 \end{aligned}$$

which is just the difference between the peak amplitude of the convolution and the amplitude a time δt away from the peak. (The third line is derived from the second by shuffling the negative and positive frequency components around.) The expression vanishes if $\delta t = 0$; *i.e.*, if the peak of the convolution coincides with a time sample. Richard Schnee has shown that one can correct for this effect by using multiple templates, shifted by time offsets smaller than Δt . The implementation of this for Run 19 is discussed in Chapter 6.

Appendix C

Phonon-System Misbehavior

A number of possible manifestations of a problem with the BLIP phonon channels were seen during Runs 19A and 19B, as indicated in the run chronologies presented in Chapter 7. The symptoms became progressively worse during May, 1999, until it was necessary to stop taking data on June 4 and study the problem intensively. Two different symptoms were encountered:

- The primary symptom, which began appearing on April 13, was outbursts in the phonon-trigger rate due to significantly increased noise in one or more detectors' phonon channels. There were two forms of this symptom:
 - Excess low-frequency noise, typically only increasing the noise below about 100 Hz.
 - Periodic events, with slow rise times suggesting “thermophonic” (microphonics depositing mechanical energy in the detectors, yielding a thermal signal) origin. The episodes were transient and the pulses varying in amplitude during an episode, with pulses correlated between detectors. The events were strikingly periodic, though the actual frequency was seen to vary. There appear to have been two modes, one around 10 Hz and another around 1 Hz.
- On or around December 4, 1998, the phonon pulses of all the detectors became “slow” — all the rise and fall times increased by a factor of a few. However, the pulses generated by the IBAPACAP appeared unchanged from the standard shape. The DC refs were normal, indicating the thermistor temperatures were no different from normal, and did not change when the IBAPACAP was enabled. This symptom recurred in BLIPs 1 and 2 on May 28, 1999; they were turned off in response. It recurred again during the studies that began June 4, 1999.

Furthermore, when any of the above symptoms occurred, they tended to occur in more than one detector at a time, though typically an onset was seen in one detector, then another, and so on.

It was found that, in all cases, a “LED bake” (turning on the LEDs used for neutralization for 20 minutes) ended the episodes, though, over time, the quiescent period thereby induced decreased in length from many days to less than an hour. A LED bake not only deposits an enormous number of photons into the detectors, but also deposits of order 1 mW for 20 minutes into the

detectors and their mounting hardware. This heating raises the entire mixing-chamber layer of the Icebox up to hundreds of mK. Similar quiescent periods, though less long-lived, were obtained by cycling the AC power on the front-end electronics, which also dumps a large amount of power into the refrigerator as the amplifiers find their quiescent state. This type of recovery was only seen if the electronics were cycled with the Detector I/O cables (the cables connecting the electronics to the detector striplines) connected, indicating that the symptoms were not simply due to the electronics boards finding some anomalous state. Even more convincingly, it was found that applying power directly to the detectors by applying a DC current to the IBAPACAP pulser on the detector, which results in a heating of the detector alone, momentarily alleviated the slow pulse problem, but the symptoms reappeared as the detector cooled down to its original temperature. This test was not tried during a noise episode.

In parallel with the above observations, a number of other possible causes were explored. In Run 18, ice in the liquid nitrogen bath caused bubbling that gave rise to thermophonic events. The bubbling could be prevented by allowing the LN bath to pressurize. This was tried and had no effect on the outbursts. Furthermore, LED baking, which did work, dumps a negligible power into the LN layer and so would be unable to affect a bubbling problem.

Another frequent microphonics suspect in dilution refrigerators is the pot needle valve. This valve permits a minute flow of LHe from the bath into the pot to replenish the helium that is pumped off. The flow of the liquid through the valve is known to give rise to microphonics seen in both the test facility and the Icebox previously via noise in the ionization circuits. Closing the pot needle valve temporarily relieves such microphonics by stopping the liquid flow, and this was attempted, to no effect. However, the pot cannot be completely ruled out as a cause because LED baking dumps enough power into the refrigerator to raise the pot pressure from its usual 0.8–0.9 mm Hg to a few mm Hg. Such a drastic change in the pot state could easily affect the flow of liquid from the bath.

Given that the observed symptoms could also be caused by electronics problems, some detectors were switched back to the 3U-format front-end electronics used in previous runs. This was done in the midst of a periodic pulse episode. By turning on the AC power with the Detector I/O cables disconnected and then plugging in the cables, one can avoid dumping significant power into the detectors. This was done to avoid killing the symptoms via the power cycle. The periodic pulsing remained with the 3U electronics. Furthermore, after a power cycle to alleviate the periodic pulsing, the detectors fell into the “slow pulse” state and slow pulses were seen from detectors connected to both 3U and 9U electronics.

To check the thermal state of the detectors, a 10-Hz square-wave bias, offset so as to apply zero power during half of the cycle, was applied to one thermistor of one detector and the other thermistor was observed with the standard 1-kHz sine wave and lockin setup. The slow square-wave bias provides a periodic power input that cycles the crystal temperature with sharp transitions. The rise and fall times observed in the second thermistor were typical of standard pulse time constants, indicating the heat capacities and conductances of the thermal circuit were at the nominal values. This result is reasonable, as it is analogous to the observation of normally shaped events from IBAPACAP pulses.

Finally, there was already an expectation of large amounts of He gas in the IVC. During both the Run 19A and 19B LHe cooldowns, helium was allowed to condense in the bath while the IVC pressure of He exchange gas was quite high, tens to 100 mT. Once liquid has condensed,

the He exchange gas becomes so cold that a standard turbopump cannot remove it. This was indeed observed — the IVC pressure remained in the vicinity of 3 mT for all of Run 19B in spite of continual turbopumping. Furthermore, a leak detector connected to the IVC observed a sharp ($> 10\times$) increase in the ^4He leak rate during He transfers (though no change in IVC pressure was observed). Thus, additional He was being allowed into the IVC over time. In addition, sudden IVC pressure excursions (going up to tens of mT from the 3 mT baseline) were observed. The reality of the excursions was confirmed by correlated increases in base temperature due to the increased thermal conductance between the mixing-chamber and higher-temperature layers.

The most plausible explanation so far found for these symptoms is that the high ^4He pressure in the IVC led to condensation of He onto the detectors. For this explanation to work, the resulting superfluid helium film must be decoupled from the thermal phonons generated by any of the various electrical heating mechanisms, but must be well coupled to the athermal phonons produced initially by particle interactions. Presumably, the He film could absorb athermal phonons and convert their energy into long-lived excitations. If the decay of these excitations occurs over tens of ms, they would return the absorbed energy to the detector very slowly, resulting in slow pulses. IBAPACAP pulsing and square-wave thermistor biasing would not produce athermal phonons and thus would exhibit their normal behaviors. The noise and periodic pulsing observed might be explained by evaporation and recondensation of He on the detectors, or even macroscopic dripping. The assorted heating impulses (LED bakes, power cycles, DC bias of IBAPACAP) would deposit enough power to temporarily evaporate the films, but He would recondense on the cold, clean detector surfaces soon — an empty surface in the presence of so much He gas is not an equilibrium situation.

Based on these arguments, the Icebox was cycled to room temperature during June and re-cooled, being careful to achieve a lower He pressure in the IVC before condensation of LHe. The residual exchange-gas pressure was approximately 10 mT when liquid was condensed during the cooldown, about an order of magnitude less than the previous cooldown. Only one phonon-trigger outburst was observed during the three months of Run 19C.

Appendix D

Veto-Anticoincident Nuclear-Recoil Event Parameters

This appendix contains a list of event parameters for each of the 13 single-scatter and 4 multiple-scatter nuclear recoils. The parameter lists also indicate whether the event passes various cuts (defined in Chapter 7) by a 0 or 1 for event parameters beginning with “c.” The definitions of the event parameters are as listed in Table D.1.

SeriesNumber	number of file series, in the form YYMMDDHHMM
EventNumber	event number in series
EventTime	time of event, in Macintosh seconds (seconds since Jan 1, 1904)
LiveTime	time between enabling of trigger and event trigger [ms]
TimeBetween	time between event trigger of this event and the previous event [ms]
LastISRTTime	time since last front-end subrack command control [s]
VTPreTimeFast	time between event trigger and last veto trigger [μ s]
VTNearQTime	difference between event time, as determined from ionization delay, and nearest veto trigger [μ s]
VTNearPTime	difference between event time, as determined from phonon delay, and nearest veto trigger [μ s]
VetoXXXHigh	XXX veto side pulse integral in the ADC triggered by veto high trigger (not available for Runs 19A/B)
VetoXXXLow	XXX veto side pulse integral in the ADC triggered by veto window trigger (not available for Runs 19A/B)
pri	recoil energy calculated using inner-electrode ionization signal only; valid for cQinOnly events [keV]
qi	inner-electrode ionization energy [keV]
pr	recoil energy calculated using summed ionization signal [keV]
qsum	summed ionization signal [keV]
qo	outer-electrode ionization energy [keV]
qpart	ionization partition, (qi - qo)/qsum
pheat	phonon energy [keV]
P1bs, P2bs	mean of phonon pretrigger baseline [digitizer bins]
P1std, P2std	standard deviation of phonon pretrigger baseline [digitizer bins]
cQTrig	1 if ionization trigger occurred for the given detector at trigger time
cPTrig	1 if phonon trigger occurred for the given detector at trigger time
QPreTime	time of last ionization trigger prior to event trigger [μ s]. Can be small (-1 μ s) and negative for triggers coincident with event trigger. -99999 indicates timeout.
QPostTime	time of first ionization trigger after event trigger [μ s]. Can be small and positive for coincident events. 99999 indicates timeout.
PPostTime	time of first phonon trigger after event trigger [μ s]. For ionization triggers, this is typically 2000–4000 μ s because of the slow rise of the phonon pulse. Becomes later as the phonon energy decreases (pulse slewing effect). 99999 indicates timeout.

Table D.1: Definitions of event parameters.

single scatter 1

```

SeriesNumber = 9903232041   EventNumber = 130628
EventTime = 3005118847
LiveTime = 1753   TimeBetween = 1985   LastISRTTime = 402
VTPreTimeFast = -268   VTNearQTime = 201   VTNearPTime = 3889
VetoTopHigh      -999999
VetoTopLow       -999999
VetoCrackHigh    -999999
VetoCrackLow     -999999
VetoNorthHigh    -999999
VetoNorthLow     -999999
VetoSouthHigh    -999999
VetoSouthLow     -999999
VetoEastHigh     -999999
VetoEastLow      -999999
VetoWestHigh     -999999
VetoWestLow      -999999
VetoBottomHigh   -999999
VetoBottomLow    -999999
VetoORHigh       -999999
VetoORLow        -999999
quantity         103      104      105      106
-----
pri              0.01     -0.12     -0.48     55.16
qi              -0.09      0.01      0.27     19.68
pr               0.53      0.79     -0.21     55.13
qsum            -0.35     -0.45      0.14     19.70
qo              -0.26     -0.46     -0.14      0.02
qpart           -0.47     -1.06      2.99      1.00
pheat           -0.17     -0.10      0.07     94.52

cQinThresh      0         0         0         1
cQoutNoise      1         1         1         1
cQsumThresh     0         0         0         1
cQinOnly        0         0         0         1
cQoutOnly       0         0         0         0
cQShare         0         0         0         0

cQinNR          1         1         1         1
cQNR            1         1         1         1

cGoodTime       1         1         1         1
cPreQual        1         1         1         1
cBaseQual       0         0         0         1
cDataQual       0         0         0         1

Plbs            580.87    605.50    743.36    685.13
P2bs            561.35    593.28    687.19    696.33
Plstd           1.22     1.43     1.27     1.60
P2std           1.43     1.11     1.33     1.82

cQTrig          0         0         0         1
cPTrig          0         0         0         0
QPreTime        -99999    -99999    -99999    -99999
QPostTime       99999    99999    99999    99999
PPostTime       99999    99999    99999    2543

```

APPENDIX D. VETO-ANTICOINCIDENT NUCLEAR-RECOIL EVENT PARAMETERS

432

single scatter 2

```

SeriesNumber = 9903232041   EventNumber = 160980
EventTime = 3005125243
LiveTime = 1075   TimeBetween = 1302   LastISRTTime = 1130
VTPreTimeFast = -388   VTNearQTime = -45.2   VTNearPTime = 167
VetoTopHigh      -999999
VetoTopLow       -999999
VetoCrackHigh    -999999
VetoCrackLow     -999999
VetoNorthHigh    -999999
VetoNorthLow     -999999
VetoSouthHigh    -999999
VetoSouthLow     -999999
VetoEastHigh     -999999
VetoEastLow      -999999
VetoWestHigh     -999999
VetoWestLow      -999999
VetoBottomHigh   -999999
VetoBottomLow    -999999
VetoORHigh       -999999
VetoORLow        -999999
quantity          103          104          105          106
-----
pri              0.56          1.22          0.91          13.55
qi              -0.02          0.04         -0.44           1.77
pr               0.03         -0.21          0.86          12.18
qsum             0.24          0.75         -0.42           2.46
qo               0.26          0.71          0.02           0.69
qpart           -1.17         -0.90          1.11           0.44
pheat            0.52          1.29          0.02          17.10

cQinThresh        0            0            0            1
cQoutNoise        1            0            1            1
cQsumThresh       0            0            0            1
cQinOnly          0            0            0            1
cQoutOnly         0            0            0            0
cQShare           0            0            0            0

cQinNR            1            1            1            1
cQNR              1            0            1            1

cGoodTime         1            1            1            1
cPreQual          1            1            1            1
cBaseQual         0            0            0            1
cDataQual         0            0            0            1

P1bs              677.66        705.00        691.85        706.39
P2bs              647.10        693.58        626.60        711.18
P1std              1.43          1.30          1.14           1.59
P2std              1.48          1.49          1.38           2.56

cQTrig            0            0            0            0
cPTrig            0            0            0            1
QPreTime         -999999        -999999        -999999        -999999
QPostTime         999999         999999         999999         999999
PPostTime         999999         999999         999999         999999

```

single scatter 3

```

SeriesNumber = 9904141258   EventNumber = 240254
EventTime = 3007002813
LiveTime = 336   TimeBetween = 569   LastISRTime = 1448
VTPreTimeFast = -105   VTNearQTime = 66.8   VTNearPTime = -118
VetoTopHigh      -999999
VetoTopLow       -999999
VetoCrackHigh    -999999
VetoCrackLow     -999999
VetoNorthHigh    -999999
VetoNorthLow     -999999
VetoSouthHigh    -999999
VetoSouthLow     -999999
VetoEastHigh     -999999
VetoEastLow      -999999
VetoWestHigh     -999999
VetoWestLow      -999999
VetoBottomHigh   -999999
VetoBottomLow    -999999
VetoORHigh       -999999
VetoORLow        -999999
quantity         103         104         105         106
-----
pri              0.30        -0.20         0.10        38.43
qi              -0.09         0.10        -0.08        12.85
pr               0.08         0.52        -0.36        39.34
qsum             0.02        -0.26         0.15        12.39
qo               0.11        -0.36         0.23        -0.45
qpart           -9.54        -1.76        -1.99         1.07
pheat            0.12        -0.00        -0.05        64.12

cQinThresh       0           0           0           1
cQoutNoise       1           1           1           1
cQsumThresh      0           0           0           1
cQinOnly         0           0           0           1
cQoutOnly        0           0           0           0
cQShare          0           0           0           0

cQinNR           1           1           1           1
cQNR             1           1           1           1

cGoodTime        1           1           1           1
cPreQual         1           1           1           1
cBaseQual        0           0           0           1
cDataQual        0           0           0           1

Plbs             502.63      327.15      469.72      557.09
P2bs             466.53      320.74      397.12      562.97
Plstd            1.39         1.48         1.26         1.39
P2std            1.29         1.45         1.26         1.22

cQTrig           0           0           0           1
cPTrig           0           0           0           0
QPreTime         -999999      -999999      -999999      -999999
QPostTime        99999      99999      99999      99999
PPostTime        99999      99999      99999      3503

```

APPENDIX D. VETO-ANTICOINCIDENT NUCLEAR-RECOIL EVENT PARAMETERS

434

single scatter 4

```

SeriesNumber = 9904151325   EventNumber = 410598
EventTime = 3007107389
LiveTime = 1459   TimeBetween = 1723   LastISRTTime = 259
VTPreTimeFast = -894   VTNearQTime = 193.8   VTNearPTime = 1027
VetoTopHigh      -999999
VetoTopLow       -999999
VetoCrackHigh    -999999
VetoCrackLow     -999999
VetoNorthHigh    -999999
VetoNorthLow     -999999
VetoSouthHigh    -999999
VetoSouthLow     -999999
VetoEastHigh     -999999
VetoEastLow      -999999
VetoWestHigh     -999999
VetoWestLow      -999999
VetoBottomHigh   -999999
VetoBottomLow    -999999
VetoORHigh       -999999
VetoORLow        -999999
quantity         103      104      105      106
-----
pri              0.72      0.45      0.65      23.95
qi               0.66     -0.04     -0.19      7.86
pr              1.24      0.76      0.66     23.83
qsum             0.39     -0.19     -0.19      7.92
qo             -0.26     -0.15     -0.00      0.06
qpart            2.34     -0.58      0.95      0.98
pheat            2.03      0.37      0.28     39.67

cQinThresh       0         0         0         1
cQoutNoise       1         1         1         1
cQsumThresh      0         0         0         1
cQinOnly         0         0         0         1
cQoutOnly        0         0         0         0
cQShare          0         0         0         0

cQinNR           1         1         1         1
cQNR             1         1         1         1

cGoodTime        1         1         1         1
cPreQual         1         1         1         1
cBaseQual        0         0         0         1
cDataQual        0         0         0         1

P1bs             80.13     21.45     258.19     186.55
P2bs             41.34     29.83     161.38     182.39
P1std            1.42      1.08      1.16      1.42
P2std            0.98      1.37      2.53      1.36

cQTrig           0         0         0         1
cPTrig           0         0         0         0
QPreTime        -999999   -999999   -999999   -999999
QPostTime       999999   999999   999999   999999
PPostTime       7098     999999   999999   3680

```

single scatter 5

```

SeriesNumber = 9904291555   EventNumber = 50264
EventTime = 3008279046
LiveTime = 558   TimeBetween = 800   LastISRTime = 737
VTPreTimeFast = -252   VTNearQTime = 75   VTNearPTime = 1013
VetoTopHigh      -999999
VetoTopLow       -999999
VetoCrackHigh    -999999
VetoCrackLow     -999999
VetoNorthHigh    -999999
VetoNorthLow     -999999
VetoSouthHigh    -999999
VetoSouthLow     -999999
VetoEastHigh     -999999
VetoEastLow      -999999
VetoWestHigh     -999999
VetoWestLow      -999999
VetoBottomHigh   -999999
VetoBottomLow    -999999
VetoORHigh       -999999
VetoORLow        -999999
quantity         103         104         105         106
-----
pri              0.11        26.72        -0.27        -1.27
qi               0.06         8.50         0.09         0.59
pr               0.66        27.86         0.37         0.05
qsum            -0.22         7.92        -0.22        -0.06
qo              -0.28        -0.57        -0.32        -0.66
qpart           -1.55         1.14        -1.82       -20.01
pheat            0.23        43.71        -0.08        -0.08

cQinThresh       0           1           0           0
cQoutNoise       1           1           1           1
cQsumThresh      0           1           0           0
cQinOnly         0           1           0           0
cQoutOnly        0           0           0           0
cQShare          0           0           0           0

cQinNR           1           1           1           0
cQNR             1           1           1           1

cGoodTime        1           1           1           1
cPreQual         1           1           1           1
cBaseQual        0           1           0           0
cDataQual        0           1           0           0

Plbs             452.50       380.22       451.17       460.75
P2bs             415.28       375.79       376.10       463.69
Plstd            1.31         1.28         1.11         1.38
P2std            1.28         1.50         1.35         1.38

cQTrig           0           1           0           0
cPTrig           0           0           0           0
QPreTime         -999999      -999999      -999999      -999999
QPostTime        99999       99999       99999       99999
PPostTime        99999       3023        99999       99999

```

APPENDIX D. VETO-ANTICOINCIDENT NUCLEAR-RECOIL EVENT PARAMETERS

436

single scatter 6

```

SeriesNumber = 9905021512   EventNumber = 290639
EventTime = 3008577524
LiveTime = 1220   TimeBetween = 1448   LastISRTTime = 293
VTPreTimeFast = -216   VTNearQTime = 67.8   VTNearPTime = 4174
VetoTopHigh      -999999
VetoTopLow       -999999
VetoCrackHigh    -999999
VetoCrackLow     -999999
VetoNorthHigh    -999999
VetoNorthLow     -999999
VetoSouthHigh    -999999
VetoSouthLow     -999999
VetoEastHigh     -999999
VetoEastLow      -999999
VetoWestHigh     -999999
VetoWestLow      -999999
VetoBottomHigh   -999999
VetoBottomLow    -999999
VetoORHigh       -999999
VetoORLow        -999999
quantity          103      104      105      106
-----
pri              -0.02      0.23     -0.12     23.86
qi               -0.18      0.17      0.26      5.42
pr              -1.08      0.32     -0.15     23.16
qsum             0.35      0.12      0.28      5.77
qo               0.53     -0.05      0.02      0.35
qpart            -2.06      1.76      0.88      0.88
pheat            -0.39      0.56      0.41     34.70

cQinThresh       0         0         0         1
cQoutNoise       1         1         1         1
cQsumThresh      0         0         0         1
cQinOnly         0         0         0         1
cQoutOnly        0         0         0         0
cQShare          0         0         0         0

cQinNR           1         1         1         1
cQNR             1         1         1         1

cGoodTime        1         1         1         1
cPreQual         1         1         1         1
cBaseQual        0         0         0         1
cDataQual        0         0         0         1

Plbs             968.01    896.64    920.31    929.51
P2bs             935.87    871.38    874.76    937.61
Plstd            1.36      1.61      1.05      1.85
P2std            1.46      1.78      1.05      1.86

cQTrig           0         0         0         1
cPTrig           0         0         0         0
QPreTime         -99999    -99999    -99999    -99999
QPostTime        99999    99999    99999    99999
PPostTime        99999    99999    99999    3109

```


single scatter 7

```

SeriesNumber = 9905131333   EventNumber = 90702
EventTime = 3009487068
LiveTime = 570   TimeBetween = 833   LastISRTime = 185
VTPreTimeFast = -164   VTNearQTime = 134.4   VTNearPTime = 2621
VetoTopHigh      -999999
VetoTopLow       -999999
VetoCrackHigh    -999999
VetoCrackLow     -999999
VetoNorthHigh    -999999
VetoNorthLow     -999999
VetoSouthHigh    -999999
VetoSouthLow     -999999
VetoEastHigh     -999999
VetoEastLow      -999999
VetoWestHigh     -999999
VetoWestLow      -999999
VetoBottomHigh   -999999
VetoBottomLow    -999999
VetoORHigh       -999999
VetoORLow        -999999
quantity         103         104         105         106
-----
pri              0.34        15.67         0.23         0.61
qi              -0.09         4.37        -0.24        -0.32
pr               0.55        15.15         1.16         0.03
qsum            -0.19         4.62        -0.70        -0.03
qo              -0.10         0.26        -0.46         0.29
qpart           -0.05         0.89        -0.32        19.09
pheat           0.16        24.40        -0.24        -0.04

cQinThresh       0           1           0           0
cQoutNoise       1           1           1           1
cQsumThresh      0           1           0           0
cQinOnly         0           1           0           0
cQoutOnly        0           0           0           0
cQShare          0           0           0           0

cQinNR           1           1           1           1
cQNR             1           1           1           1

cGoodTime        1           1           1           1
cPreQual         1           1           1           1
cBaseQual        0           1           0           0
cDataQual        0           1           0           0

Plbs             538.61      417.18      585.89      560.04
P2bs             508.15      414.48      508.78      559.02
Plstd            1.25       1.41       1.27       1.45
P2std            1.24       1.56       1.23       1.35

cQTrig           0           1           0           0
cPTrig           0           0           0           0
QPreTime         -99999     -99999     -99999     -99999
QPostTime        99999      99999      99999      99999
PPostTime        99999      3385      99999      99999

```

APPENDIX D. VETO-ANTICOINCIDENT NUCLEAR-RECOIL EVENT PARAMETERS

438

single scatter 8

```

SeriesNumber = 9905191346   EventNumber = 140408
EventTime = 3010021639
LiveTime = 2322   TimeBetween = 2518   LastISRTTime = 240
VTPreTimeFast = -30   VTNearQTime = -31.6   VTNearPTime = -163
VetoTopHigh      -999999
VetoTopLow       -999999
VetoCrackHigh    -999999
VetoCrackLow     -999999
VetoNorthHigh    -999999
VetoNorthLow     -999999
VetoSouthHigh    -999999
VetoSouthLow     -999999
VetoEastHigh     -999999
VetoEastLow      -999999
VetoWestHigh     -999999
VetoWestLow      -999999
VetoBottomHigh   -999999
VetoBottomLow    -999999
VetoORHigh       -999999
VetoORLow        -999999
quantity          103          104          105          106
-----
pri              -0.73         82.19         0.66         -0.54
qi               0.30         25.72        -0.33          0.45
pr              -0.44         81.56        -0.98         -1.29
qsum             0.15         26.03         0.49          0.82
qo              -0.15          0.32          0.82          0.37
qpart            2.99          0.98         -2.36          0.09
pheat           -0.14        133.61        -0.01          0.35

cQinThresh       0           1           0           0
cQoutNoise       1           1           0           1
cQsumThresh      0           1           0           0
cQinOnly         0           1           0           0
cQoutOnly        0           0           0           0
cQShare          0           0           0           0

cQinNR           1           1           1           1
cQNR             1           1           1           0

cGoodTime        1           1           1           1
cPreQual         1           1           1           1
cBaseQual        0           1           0           0
cDataQual        0           1           0           0

Plbs             501.75        487.00        604.33        541.75
P2bs             463.96        475.84        536.40        550.81
Plstd            1.43          1.39          1.02          1.78
P2std            1.24          1.19          1.57          1.59

cQTrig           0           1           0           0
cPTrig           0           0           0           0
QPreTime         -999999        -999999        -999999        -999999
QPostTime        99999          99999          99999          99999
PPostTime        99999          2652          99999          99999

```

single scatter 9

```

SeriesNumber = 9906021605   EventNumber = 140863
EventTime = 3011241504
LiveTime = 6266   TimeBetween = 6529   LastISRTTime = 278
VTPreTimeFast = -185   VTNearQTime = 176.8   VTNearPTime = -490
VetoTopHigh      -999999
VetoTopLow       -999999
VetoCrackHigh    -999999
VetoCrackLow     -999999
VetoNorthHigh    -999999
VetoNorthLow     -999999
VetoSouthHigh    -999999
VetoSouthLow     -999999
VetoEastHigh     -999999
VetoEastLow      -999999
VetoWestHigh     -999999
VetoWestLow      -999999
VetoBottomHigh   -999999
VetoBottomLow    -999999
VetoORHigh       -999999
VetoORLow        -999999
quantity         103      104      105      106
-----
pri              0.03     22.58     0.37     -0.10
qi               0.00      6.04     -0.30      0.09
pr               1.02     23.20      0.89      0.37
qsum             -0.49      5.73     -0.56     -0.14
qo               -0.49     -0.31     -0.26     -0.23
qpart            -1.01      1.11      0.07     -2.31
pheat            0.04     34.66     -0.22      0.09

cQinThresh       0         1         0         0
cQoutNoise       1         1         1         1
cQsumThresh      0         1         0         0
cQinOnly         0         1         0         0
cQoutOnly        0         0         0         0
cQShare          0         0         0         0

cQinNR           1         1         1         1
cQNR             1         1         1         1

cGoodTime        1         1         1         1
cPreQual         1         1         1         1
cBaseQual        0         1         0         0
cDataQual        0         1         0         0

Plbs             602.31    611.24    772.85    794.50
P2bs             568.85    595.42    716.03    799.68
Plstd            1.25      1.30      1.25      1.19
P2std            1.33      1.66      1.23      1.72

cQTrig           0         1         0         0
cPTrig           0         0         0         0
QPreTime         -99999   -99999   -99999   -99999
QPostTime        99999   99999   99999   99999
PPostTime        99999   3036    99999   99999

```

APPENDIX D. VETO-ANTICOINCIDENT NUCLEAR-RECOIL EVENT
PARAMETERS

440

single scatter 10

```

SeriesNumber = 9907281402   EventNumber = 340427
EventTime = 3016119623
LiveTime = 4818   TimeBetween = 4987   LastISRTTime = 45922
VTPreTimeFast = -324   VTNearQTime = 438.6   VTNearPTime = 413
VetoTopHigh      0
VetoTopLow       0
VetoCrackHigh    0
VetoCrackLow     0
VetoNorthHigh    0
VetoNorthLow     0
VetoSouthHigh    0
VetoSouthLow     0
VetoEastHigh     0
VetoEastLow      0
VetoWestHigh     0
VetoWestLow      0
VetoBottomHigh   0
VetoBottomLow    0
VetoORHigh       0
VetoORLow        0
quantity         103      104      105      106
-----
pri              -0.36      0.12     15.22      0.82
qi               0.02     -0.06      4.55     -0.60
pr              -0.85      1.14     15.31      0.24
qsum             0.26     -0.57      4.50     -0.31
qo              0.25     -0.51     -0.05      0.29
qpart           -0.87     -0.78      1.02      2.90
pheat           -0.33     -0.00     24.31     -0.37

cQinThresh       0         0         1         0
cQoutNoise       1         1         1         1
cQsumThresh      0         0         1         0
cQinOnly         0         0         1         0
cQoutOnly        0         0         0         0
cQShare          0         0         0         0

cQinNR           1         1         1         1
cQNR             1         1         1         1

cGoodTime        1         1         1         1
cPreQual         1         1         1         1
cBaseQual        0         0         1         0
cDataQual        0         0         1         0

Plbs             672.62    670.82    682.23    667.68
P2bs            631.10    659.00    616.42    671.39
Plstd            1.80      1.35      1.11      1.24
P2std            1.27      1.59      1.18      2.03

cQTrig           0         0         0         0
cPTrig           0         0         1         0
QPreTime        -99999    -99999    -99999    -4813862
QPostTime       99999     99999     99999     99999
PPostTime       99999     99999     99999     99999

```

single scatter 11

```

SeriesNumber = 9907311450   EventNumber = 190309
EventTime = 3016345204
LiveTime = 806   TimeBetween = 1041   LastISRTime = 257
VTPreTimeFast = -482   VTNearQTime = 93.4   VTNearPTime = -482
VetoTopHigh      0
VetoTopLow       0
VetoCrackHigh    0
VetoCrackLow     0
VetoNorthHigh    0
VetoNorthLow     0
VetoSouthHigh    0
VetoSouthLow     0
VetoEastHigh     0
VetoEastLow      0
VetoWestHigh     0
VetoWestLow      0
VetoBottomHigh   0
VetoBottomLow    0
VetoORHigh       0
VetoORLow        0
quantity         103         104         105         106
-----
pri              0.32        -0.33        45.98         0.86
qi              -0.17         0.27        15.05        -0.41
pr               0.24        -0.29        45.66         0.72
qsum            -0.13         0.25        15.21        -0.34
qo               0.04        -0.02         0.16         0.07
qpart           1.58         1.16         0.98         1.40
pheat           -0.01         0.21        76.08         0.03

cQinThresh      0           0           1           0
cQoutNoise      1           1           1           1
cQsumThresh     0           0           1           0
cQinOnly        0           0           1           0
cQoutOnly       0           0           0           0
cQShare         0           0           0           0

cQinNR          1           1           1           1
cQNR            1           1           1           1

cGoodTime       1           1           1           1
cPreQual        1           1           1           1
cBaseQual       0           0           1           0
cDataQual       0           0           1           0

Plbs            377.43       417.69       523.47       536.32
P2bs            338.59       406.63       445.97       542.27
Plstd           1.57         1.22         1.12         1.44
P2std           1.26         1.25         1.59         1.48

cQTrig          0           0           1           0
cPTrig          0           0           0           0
QPreTime        -99999       -99999       -99999       -99999
QPostTime       99999       99999       99999       99999
PPostTime       99999       99999       2627        99999

```

APPENDIX D. VETO-ANTICOINCIDENT NUCLEAR-RECOIL EVENT PARAMETERS

442

single scatter 12

```

SeriesNumber = 9908201410   EventNumber = 110537
EventTime = 3018053934
LiveTime = 4543   TimeBetween = 4752   LastISRTTime = 1289
VTPreTimeFast = -27   VTNearQTime = -27   VTNearPTime = -479
VetoTopHigh      0
VetoTopLow       0
VetoCrackHigh    0
VetoCrackLow     0
VetoNorthHigh    0
VetoNorthLow     0
VetoSouthHigh    0
VetoSouthLow     0
VetoEastHigh     0
VetoEastLow      0
VetoWestHigh     0
VetoWestLow      0
VetoBottomHigh   0
VetoBottomLow    0
VetoORHigh       0
VetoORLow        0
quantity         103         104         105         106
-----
pri              0.24        -0.62        -0.25        50.23
qi              -0.12         0.24         0.19        16.55
pr               0.13        -1.27        -0.23        49.60
qsum            -0.06         0.56         0.18        16.86
qo               0.05         0.33        -0.01         0.31
qpart           2.74        -0.16         1.15         0.96
pheat           0.01        -0.15         0.13        83.32

cQinThresh      0           0           0           1
cQoutNoise      1           1           1           1
cQsumThresh     0           0           0           1
cQinOnly        0           0           0           1
cQoutOnly       0           0           0           0
cQShare         0           0           0           0

cQinNR          1           1           1           1
cQNR            1           0           1           1

cGoodTime       1           1           1           1
cPreQual        1           1           1           1
cBaseQual       0           0           0           1
cDataQual       0           0           0           1

Plbs            405.54       465.90       586.38       599.55
P2bs            366.02       454.03       513.95       606.73
Plstd           1.34         1.50         1.04         1.32
P2std           1.32         1.37         1.21         1.42

cQTrig          0           0           0           1
cPTrig          0           0           0           0
QPreTime        -99999       -99999       -99999       -99999
QPostTime       99999       99999       99999       99999
PPostTime       99999       99999       99999       2822

```

single scatter 13

```

SeriesNumber = 9908261350   EventNumber = 240974
EventTime = 3018600625
LiveTime = 2896   TimeBetween = 3105   LastISRTTime = 1089
VTPreTimeFast = -242   VTNearQTime = 38.6   VTNearPTime = 77
VetoTopHigh      0
VetoTopLow       0
VetoCrackHigh    0
VetoCrackLow     0
VetoNorthHigh    0
VetoNorthLow     0
VetoSouthHigh    0
VetoSouthLow     0
VetoEastHigh     0
VetoEastLow      0
VetoWestHigh     0
VetoWestLow      0
VetoBottomHigh   0
VetoBottomLow    0
VetoORHigh       0
VetoORLow        0
quantity         103         104         105         106
-----
pri              -0.57        1.31        11.02        -0.24
qi               0.14        -0.67         3.30         0.05
pr               0.60         0.99        10.73        -0.04
qsum             -0.44        -0.51         3.45        -0.06
qo              -0.58         0.16         0.15        -0.10
qpart            -1.64         1.62         0.92        -2.61
pheat            -0.29        -0.03        17.63        -0.15

cQinThresh       0           0           1           0
cQoutNoise       0           1           1           1
cQsumThresh      0           0           1           0
cQinOnly         0           0           1           0
cQoutOnly        0           0           0           0
cQShare          0           0           0           0

cQinNR           1           1           1           1
cQNR             1           1           1           1

cGoodTime        0           1           1           1
cPreQual         0           1           1           1
cBaseQual        0           0           1           0
cDataQual        0           0           1           0

Plbs             481.98       459.98       549.63       565.47
P2bs             440.38       450.29       474.16       570.25
Plstd            1.18         1.31         1.19         1.10
P2std            1.11         1.36         1.13         1.54

cQTrig           0           0           0           0
cPTrig           0           0           1           0
QPreTime         -99999       -99999       -99999       -99999
QPostTime        99999       99999       99999       99999
PPostTime        99999       99999       99999       99999

```

APPENDIX D. VETO-ANTICOINCIDENT NUCLEAR-RECOIL EVENT
PARAMETERS

444

multiple scatter 1

```

SeriesNumber = 9903081411   EventNumber = 90278
EventTime = 3003791803
LiveTime = 2730   TimeBetween = 2941   LastISRTTime = 294
VTPreTimeFast = -141   VTNearQTime = -134.6   VTNearPTime = 1355
VetoTopHigh      -999999
VetoTopLow       -999999
VetoCrackHigh    -999999
VetoCrackLow     -999999
VetoNorthHigh    -999999
VetoNorthLow     -999999
VetoSouthHigh    -999999
VetoSouthLow     -999999
VetoEastHigh     -999999
VetoEastLow      -999999
VetoWestHigh     -999999
VetoWestLow      -999999
VetoBottomHigh   -999999
VetoBottomLow    -999999
VetoORHigh       -999999
VetoORLow        -999999
quantity         103         104         105         106
-----
pri              0.73         0.05        13.78        12.15
qi              -0.49        -0.19         3.13         3.08
pr              0.46         0.12        13.15        12.74
qsum            -0.28        -0.24         3.60         2.63
qo              0.20        -0.05         0.47        -0.45
qpart           2.42         0.60         0.74         1.34
pheat           0.08        -0.21        17.95        16.25

cQinThresh      0           0           1           1
cQoutNoise      1           1           1           1
cQsumThresh     0           0           1           1
cQinOnly        0           0           1           1
cQoutOnly       0           0           0           0
cQShare         0           0           0           0

cQinNR          1           1           1           1
cQNR            1           1           1           1

cGoodTime       0           1           1           1
cPreQual        0           1           1           1
cBaseQual       0           0           1           1
cDataQual       0           0           1           1

P1bs            1173.42      1173.48      1168.58      1124.60
P2bs            1086.16      1130.70      1142.16      1142.36
P1std            1.24         1.44         1.16         1.55
P2std            1.39         1.44         0.90         1.55

cQTrig          0           0           1           0
cPTrig          0           0           0           0
QPreTime        -999999      -999999      -999999      -999999
QPostTime       999999      999999      999999      999999
PPostTime       999999      999999      3479         3839

```


multiple scatter 2

```

SeriesNumber = 9904141258   EventNumber = 180759
EventTime = 3006993310
LiveTime = 2587   TimeBetween = 2828   LastISRTTime = 291
VTPreTimeFast = -120   VTNearQTime = 106.8   VTNearPTime = -1139
VetoTopHigh      -999999
VetoTopLow       -999999
VetoCrackHigh    -999999
VetoCrackLow     -999999
VetoNorthHigh    -999999
VetoNorthLow     -999999
VetoSouthHigh    -999999
VetoSouthLow     -999999
VetoEastHigh     -999999
VetoEastLow      -999999
VetoWestHigh     -999999
VetoWestLow      -999999
VetoBottomHigh   -999999
VetoBottomLow    -999999
VetoORHigh       -999999
VetoORLow        -999999
quantity          103          104          105          106
-----
pri              -0.13        31.22        -0.55        29.00
qi               0.07         6.46         0.08         9.62
pr              -0.63        26.57        -1.77        28.30
qsum             0.32         8.78         0.69         9.97
qo               0.25         2.33         0.61         0.35
qpart            -0.55         0.47        -0.77         0.93
pheat            0.02        44.13        -0.39        48.23

cQinThresh       0           1           0           1
cQoutNoise       1           0           1           1
cQsumThresh      0           1           0           1
cQinOnly         0           0           0           1
cQoutOnly        0           0           0           0
cQShare          0           1           0           0

cQinNR           1           0           1           1
cQNR             1           1           0           1

cGoodTime        1           1           1           1
cPreQual         1           1           1           1
cBaseQual        0           1           0           1
cDataQual        0           1           0           1

Plbs             317.10       353.58       472.75       425.61
P2bs             276.46       359.62       382.44       418.80
Plstd            1.30         1.28         1.22         1.65
P2std            1.24         1.42         1.17         2.14

cQTrig           0           1           0           0
cPTrig           0           0           0           0
QPreTime         -999999        -1        -999999     -999999
QPostTime        99999        99999        99999         1
PPostTime        99999        3041        99999        3311

```

APPENDIX D. VETO-ANTICOINCIDENT NUCLEAR-RECOIL EVENT PARAMETERS

446

multiple scatter 3

```

SeriesNumber = 9904271059   EventNumber = 200939
EventTime = 3008114831
LiveTime = 242   TimeBetween = 528   LastISRTTime = 22206
VTPreTimeFast = -39   VTNearQTime = 31.4   VTNearPTime = 731
VetoTopHigh      -999999
VetoTopLow       -999999
VetoCrackHigh    -999999
VetoCrackLow     -999999
VetoNorthHigh    -999999
VetoNorthLow     -999999
VetoSouthHigh    -999999
VetoSouthLow     -999999
VetoEastHigh     -999999
VetoEastLow      -999999
VetoWestHigh     -999999
VetoWestLow      -999999
VetoBottomHigh   -999999
VetoBottomLow    -999999
VetoORHigh       -999999
VetoORLow        -999999
quantity         103         104         105         106
-----
pri              0.53        29.00        18.72         1.37
qi              -0.44         9.33         5.46        -0.62
pr              -0.54        28.59        18.22         0.95
qsum             0.09         9.53         5.71        -0.41
qo               0.54         0.20         0.25         0.21
qpart           -10.52         0.96         0.91         2.03
pheat           -0.36        47.65        29.64         0.14

cQinThresh       0           1           1           0
cQoutNoise       1           1           1           1
cQsumThresh      0           1           1           0
cQinOnly         0           1           1           0
cQoutOnly        0           0           0           0
cQShare          0           0           0           0

cQinNR           1           1           1           1
cQNR             1           1           1           1

cGoodTime        1           1           1           1
cPreQual         1           1           1           1
cBaseQual        0           1           1           0
cDataQual        0           1           1           0

Plbs             379.52       361.99       518.08       517.65
P2bs             341.32       358.25       443.89       515.55
Plstd            1.25         1.32         1.12         1.67
P2std            1.18         1.74         1.34         1.42

cQTrig           0           1           0           0
cPTrig           0           0           0           0
QPreTime         -999999      -999999      -999999      -999999
QPostTime        99999      99999        5           99999
PPostTime        99999      2865        3135        99999

```

multiple scatter 4

```

SeriesNumber = 9905011832   EventNumber = 150696
EventTime = 3008478565
LiveTime = 4707   TimeBetween = 4967   LastISRTTime = 588
VTPreTimeFast = -42   VTNearQTime = -34   VTNearPTime = -1817
VetoTopHigh      -999999
VetoTopLow       -999999
VetoCrackHigh    -999999
VetoCrackLow     -999999
VetoNorthHigh    -999999
VetoNorthLow     -999999
VetoSouthHigh    -999999
VetoSouthLow     -999999
VetoEastHigh     -999999
VetoEastLow      -999999
VetoWestHigh     -999999
VetoWestLow      -999999
VetoBottomHigh   -999999
VetoBottomLow    -999999
VetoORHigh       -999999
VetoORLow        -999999
quantity         103         104         105         106
-----
pri              1.58        25.85        64.76         0.89
qi              -0.72        -0.03        22.95        -0.42
pr               0.41        18.10        64.69         0.22
qsum            -0.13         3.85        22.99        -0.09
qo               0.58         3.88         0.04         0.33
qpart            9.86        -1.02         1.00         8.37
pheat            0.14        25.79       110.66         0.04

cQinThresh       0          0          1          0
cQoutNoise       0          0          1          1
cQsumThresh      0          1          1          0
cQinOnly         0          0          1          0
cQoutOnly        0          1          0          0
cQShare          0          0          0          0

cQinNR           1          0          1          1
cQNR             1          1          1          1

cGoodTime        1          1          1          1
cPreQual         1          1          1          1
cBaseQual        0          1          1          0
cDataQual        0          1          1          0

Plbs             291.20       245.46       373.66       423.04
P2bs             251.03       250.65       286.01       417.95
Plstd             1.32         1.19         1.02         1.65
P2std             1.37         1.36         1.21         1.38

cQTrig           0          0          1          0
cPTrig           0          0          0          0
QPreTime        -999999      -999999      -999999      -999999
QPostTime        99999      99999      99999      99999
PPostTime        99999      3292       2523      99999

```

Appendix E

The DAMA Claim and Compatibility of DAMA and CDMS

E.1 Introduction

The DAMA collaboration has recently presented analysis of a four-year data set in which they claim to observe an annually modulated event rate characteristic of WIMP interactions. In this appendix, I discuss their claim in some detail and present an analysis of the compatibility of the DAMA and CDMS results. This is done within the framework of spin-independent WIMP-nucleon interactions. I comment on the possibility of spin-dependent interactions at the end. The work described here has been done by Rick Gaitskill, Bernard Sadoulet, Richard Schnee, and myself. Unless otherwise indicated, all information on the DAMA experiment is derived from their recent preprint on the four-year data set [88] or their 1996 exclusion-limit paper [146].

E.2 The DAMA Experiment and Annual-Modulation Claim

The DAMA (DARk MATter) experiment uses high-purity NaI(Tl) scintillation-mediated detectors to search for an annually modulated event rate characteristic of WIMP interactions. While these detectors have no intrinsic ability at low energy to discriminate WIMP-induced nuclear recoils from interactions of background particles, their large mass (~ 100 kg) and low intrinsic background-event rates make it possible to achieve the statistical precision needed to look for the unique annual-modulation signature of WIMP interactions. Annual modulation is discussed in Chapter 2. While the solar system possesses a velocity of approximately 232 km s^{-1} in the direction of the galactic disk's revolution about the center of the galaxy, the WIMPs making up the galactic halo have isotropic velocities with no net revolution. The WIMPs obey a Maxwell-Boltzmann distribution with most probable velocity $v_0 = 220 \text{ km s}^{-1}$. Therefore, for a terrestrial target, the WIMPs come primarily from the direction in which the solar system is moving. In the laboratory frame, the WIMP velocity distribution is modulated by the revolution of the Earth around the Sun, which adds or subtracts a sinusoidally varying velocity with amplitude 15 km s^{-1} to the 232 km s^{-1} solar velocity in the direction of the Sun's motion. This varying component causes the recoil-energy spectrum to be modulated with a period of 1 year. The modulation changes the average energy and overall normalization of the recoil-energy spectrum. In any given energy bin, the modulation

is well approximated by a sine wave. The phase is fixed by the orbit of the Earth, yielding maxima and minima on days 152.5 and 335, corresponding to June 1 or 2 and December 3 or 4 [77].

The DAMA experiment employs nine 9.70 kg NaI crystals, shaped as rectangular prisms, each with two low-radioactivity photomultiplier tubes viewing the crystal ends via light guides. The crystals are contained in individual low-radioactivity copper housings; the assembled detectors are housed in a low-radioactivity copper box that is surrounded by shielding consisting of concentric layers of lead, cadmium foil, and paraffin/polyethylene (innermost to outermost). The lead and copper stop photons and electrons; the paraffin and polyethylene moderate neutrons. Cadmium has a high neutron-capture cross section, so the cadmium foils also attenuate the neutron flux. The apparatus is continuously purged with high-purity N₂ gas to prevent radon from entering. The experiment is situated in the Gran Sasso National Laboratory, at a depth of 4000 mwe. At this depth, the muon flux is very small, correspondingly reducing the muon-induced electromagnetic and neutron backgrounds.

A given detector triggers if coincident pulses are seen in its two photomultiplier tubes. This yields an energy threshold in the range 1 to 2 keV “electron-equivalent,” which is proportional to the scintillation light observed. For bulk electron recoils, this energy is defined to be equal to recoil energy. Since nuclear recoils are “quenched” in NaI, the recoil energy for nuclear recoils is given by $E_R = E_{ee}/QF$ where QF is the quenching factor, 0.30 for Na recoils and 0.09 for I recoils, and E_{ee} is the electron-equivalent energy, also termed “keVee.”

Under the assumption of spin-independent interactions and a WIMP mass of tens of GeV c⁻² or higher, observable WIMP interactions occur primarily with iodine. Interactions of such a WIMP with Na are suppressed in cross section because of its low A , as was discussed in Chapter 2. Kinematic considerations also reduce the average recoil energy for Na recoils, pushing them below the threshold. For low-mass WIMPs, $\lesssim 10$ GeV c⁻², iodine is not as favored, but MSSM WIMPs below about 30 GeV c⁻² are already excluded. Furthermore, the WIMP mass that best fits the DAMA annual-modulation signal is about 50 GeV c⁻². Therefore, interactions on iodine and $QF = 0.09$ are assumed in this discussion and the recoil-energy threshold is thus between about 10 and 20 keV.

The data set published in [88] consists of a 57,986 kg d exposure obtained over a four-year period. The *efficiency-corrected* “DC” background-particle spectrum observed is shown in Figure E.1. By “efficiency-corrected,” I mean the spectrum that would be seen if the detectors had unity efficiency at all energies — the spectrum is divided by the efficiency function given in Figure E.2. Note that the spectrum is in keVee. The background-particle interaction rate is 1 to 2 keV⁻¹ kg⁻¹ d⁻¹. Conversion to recoil-energy units for nuclear recoils reduces the effective background rate by a factor $1/0.09 \approx 11$, so clearly the intrinsic background rate in these detectors is quite low, making a sensitive annual-modulation search feasible.

The “AC” signal observed in the 2-to-6-keVee energy range is shown in Figure E.3. This figure is the same as Figure 2 of [88]. I refer to the data presented in Figure E.3 as the “Figure 2” data. The AC signal is calculated as follows. The data are divided into energy bins of width 1 keVee. In each bin, the mean counting rate over the data set is determined (separate means are calculated for the first year and the remaining three years [87]). For each time bin, the difference between the observed number of counts and the number of counts expected from the mean count rate is determined. This residual is divided by the exposure for the given time bin (mass×time). The resulting count rate is corrected for efficiencies by *dividing* by the experiment’s efficiency function,

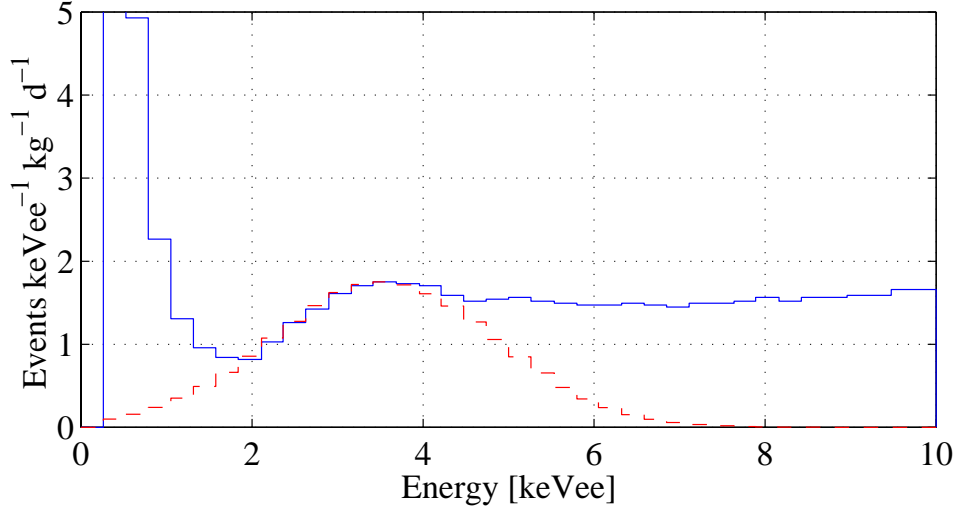


Figure E.1: Efficiency-corrected “DC” spectrum observed by the DAMA experiment with resolution function overlaid. The energy axis is in “keVee,” which corresponds to recoil energy for photons but requires division by the quenching factor (0.09) to convert to recoil-energy for nuclear recoils. The energy resolution function is $\sigma_{E_{ee}} = 0.70\sqrt{E_{ee}}$ (E_{ee} is keVee) and is derived from Figure 13 of [150].

which is shown in Figure E.2. The resulting count rates for the four energy bins between 2 and 6 keVee are *averaged* to yield Figure E.3.

This interpretation of their procedure is confirmed by checking the size of their error bars. The complete DAMA data are not available, so it is not possible to calculate the expected error bars exactly. However, the modulation amplitude is very small compared to the mean count rate shown in Figure E.1 (of order 3%), and the number of counts in a given time and energy bin is large, so the statistical uncertainty on the number of counts is given accurately by $\sqrt{\langle N \rangle}$ where $\langle N \rangle$ is the number of counts expected in the given time and energy bin from the mean counting rate. The error bars calculated in this way match those given by DAMA in Figure E.3.

Clearly, there is an annual modulation of the DAMA counting rate. To determine the best fit WIMP mass and cross section and to set a confidence region in the $(M_\delta, \sigma_{\delta n})$ plane, an approximate maximum-likelihood analysis is performed. The data are divided into 1-keVee energy bins and 1-day time bins and are separated by detector. The expected count rate due to both the DC background rate and possible WIMP interactions in the i th time interval for the j th detector in the k th energy bin is

$$\mu_{ijk} = \left[b_{jk} + S_{0,k} + S_{m,k} \cos \left(\frac{2\pi(t_i - 152.5)}{365.25} \right) \right] \Delta t_i M_j \Delta E \epsilon_{jk} \quad (\text{E.1})$$

b_{jk} is the time-independent background-particle event rate (in $\text{keV}^{-1} \text{kg}^{-1} \text{d}^{-1}$) in the j th detector and k th energy bin. $S_{0,k}$ is the mean event rate in the k th energy bin expected for a WIMP with a given M_δ and $\sigma_{\delta n}$. $S_{m,k}$ is the modulation amplitude of the WIMP event rate in the k th energy bin for the WIMP model. t_i is the time of the i th time bin. Δt_i is the width in time of the i th

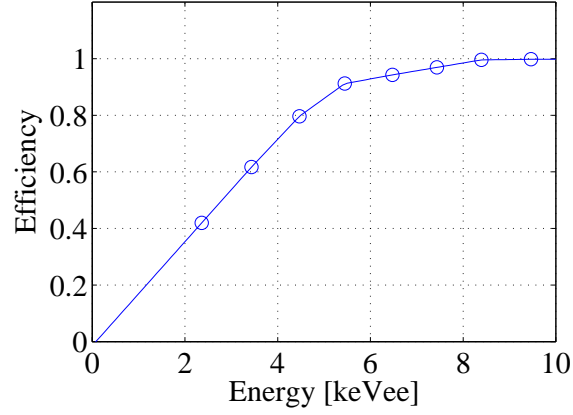


Figure E.2: DAMA efficiency function, taken from [150]. The circles indicate the data available from this reference; the line is an interpolation extrapolated to yield zero efficiency at $E_{ee} = 0$.

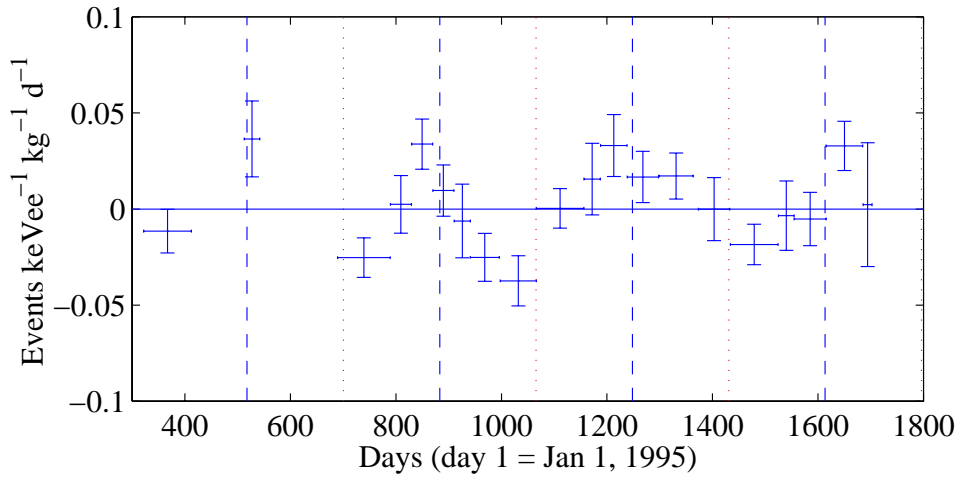


Figure E.3: Average event rate vs. time observed in the 2-to-6-keVee energy range. The horizontal axis is time in days. The error bars are DAMA's. The dashed and dotted vertical indicate the maxima and minima of the expected annual-modulation signal at days 152.5 and 335. This is Figure 2 of [88].

time bin. M_j is the mass of the j th detector. $\Delta E = 1$ keVee is the width of the energy bins. ϵ_{jk} is the efficiency of the j th detector in the k th energy bin. The cosine, of course, gives the sinusoidal modulation with the appropriate phase and period. The data are given by the ensemble of N_{ijk} , the number of counts observed in the i th time bin, in the j th detector, and in the k th energy bin. The experiment's likelihood function is given by

$$\mathcal{L}_0(N_{ijk}|b_{jk}, M_\delta, \sigma_{\delta n}) = \prod_{ijk} \frac{\mu_{ijk}^{N_{ijk}} \exp(-\mu_{ijk})}{N_{ijk}!} \quad (\text{E.2})$$

which is just a product of Poisson distribution functions with the appropriate expected numbers of counts μ_{ijk} . The function $y = -2 \log \mathcal{L}_0$ is distributed about its minimum value as χ^2 with $\nu = 2 + N_{det}N_E$ degrees of freedom, where N_{det} is the number of detectors (the j index), N_E is the number energy bins (the k index), and an additional 2 degrees of freedom arise from the WIMP mass M_δ and cross section $\sigma_{\delta n}$. During minimization of the y -function, the additional constraints $M_\delta \geq 30 \text{ GeV c}^{-2}$ and $b_{jk} \geq 0$ are applied. The first constraint applies present lower limits on the WIMP mass. The second constraint requires that no detector have a negative background rate, which seems a reasonable requirement.

The $(M_\delta, \sigma_{\delta n})$ value that minimizes y is $(52 \text{ GeV c}^{-2}, 7.2 \times 10^{-42} \text{ cm}^2)$. The b_{jk} are projected out by evaluating them at the values $\widehat{b_{jk}}$ that minimize y for the given $(M_\delta, \sigma_{\delta n})$. A 3σ CL allowed region is calculated in the standard way by finding the contour in the $(M_\delta, \sigma_{\delta n})$ plane that yields $y = \widehat{y} + 9$ where \widehat{y} is the value of the y -function at the minimum- y point $(\widehat{M_\delta}, \widehat{\sigma_{\delta n}})$. If the constraints on M_δ and b_{jk} were not applied, this 3σ CL contour would correspond to 98.9% CL because, after projecting out the b_{jk} , y is distributed about its minimum value as χ^2 with two degrees of freedom, the WIMP mass and cross section. However, the additional constraints may invalidate this correspondence. A Monte Carlo must be performed to determine exact confidence levels. DAMA do not quote an explicit percentage confidence level. The best-fit $(M_\delta, \sigma_{\delta n})$ and the 3σ CL contour are shown in Figure E.4.

It is interesting to plot the expected energy spectrum of the *modulation signal* (not the DC WIMP-interaction recoil-energy spectrum) for the best fit value of $(M_\delta, \sigma_{\delta n})$. It is straightforward to calculate the annual modulation using the formalism presented in Chapter 2. It is important, however, that the DAMA energy resolution be convolved with the expected recoil-energy spectrum because the width of the resolution function is large compared to the energies of interest, as is shown in Figure E.1. The resolution function is given in Figure 13 of [150] and takes the form $\sigma_{E_{ee}} = 0.70\sqrt{E_{ee}}$ where E_{ee} is electron-equivalent energy. The expected recoil-energy spectrum of annual modulation is converted to E_{ee} and convolved with this resolution function. The result is shown in Figure E.5.

In the same preprint that presents the four-year data set, DAMA also perform a combined analysis of the annual-modulation data and their 1996 pulse-shape-analysis exclusion limit. The intent is to use the exclusion limit to better constrain the parameters of the WIMP yielding the annual-modulation signal. They do this by adding to the y -function a term

$$\Delta y = \frac{(S_{0,k} - r_k)^2}{\sigma_k^2} \theta(S_{0,k} - r_k) \quad (\text{E.3})$$

where r_k is “the lowest counting rate in the most selective energy bin” of the data in the 1996 paper. That is, for a given M_δ and $\sigma_{\delta n}$, they pick the detector and energy bin that most severely constrains

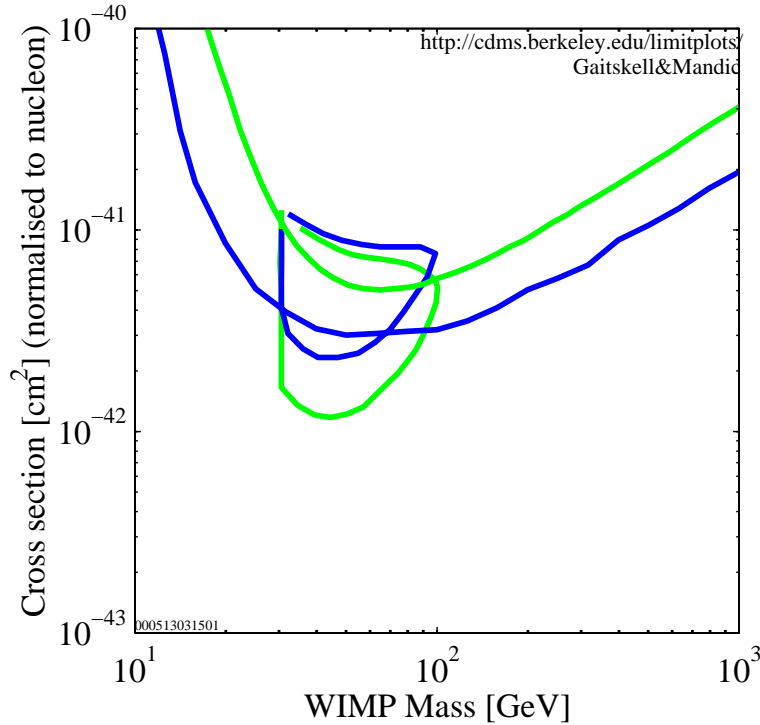


Figure E.4: DAMA allowed regions, exclusion limit, and the CDMS exclusion limit. Light solid limit line: DAMA 1996 exclusion limit. Dark solid limit line: CDMS limit. Dark heart-shaped contour: 3σ CL contour calculated from the annual-modulation analysis alone. The minimum- y point is $(M_\delta, \sigma_{\delta n}) = (52 \text{ GeV c}^{-2}, 7.2 \times 10^{-42} \text{ cm}^2)$. Light heart-shaped contour: 3σ CL contour from combined analysis of the DAMA annual-modulation data and the 1996 pulse-shape-analysis exclusion limit, yielding a minimum- y point at $(M_\delta, \sigma_{\delta n}) = (44 \text{ GeV c}^{-2}, 5.4 \times 10^{-42} \text{ cm}^2)$.

the cross section of the WIMP. σ_k is the uncertainty associated with r_k . The Heaviside function enforces the constraint only if the DC WIMP interaction rate exceeds r_k . The behavior of the likelihood function is presumably made more abnormal by this modification, so the 3σ CL contour derived from the modified y -function is certainly not a 98.9% CL confidence contour. Regardless, the analysis can be done this way, and the resulting minimum- y WIMP mass and cross section is $(M_\delta, \sigma_{\delta n}) = (44 \text{ GeV c}^{-2}, 5.4 \times 10^{-42} \text{ cm}^2)$. The 3σ CL contour from this analysis is also shown in Figure E.4.

E.3 Critique of the Annual-Modulation Claim

A number of issues arise regarding the above annual-modulation claim.

First, the DC background-event spectrum has an unexpected shape. Typically, one expects a flat background due to Compton-scattering of high-energy photons with peaks due to X-rays and a possible continuum due to electrons (from various sources) superimposed. Such a flat spectrum

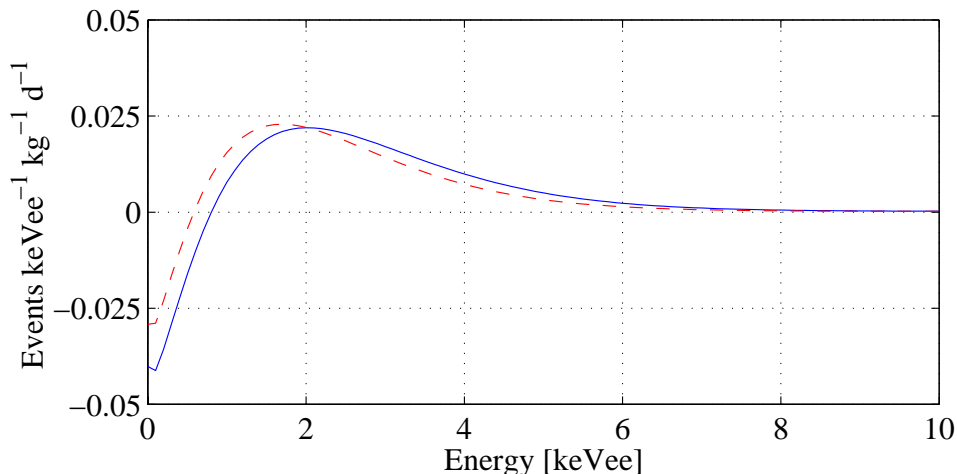


Figure E.5: Expected energy spectrum of annual-modulation signal: the difference between the energy spectrum at day 152.5 and the mean energy spectrum, giving the amplitude of the modulation as a function of energy. Note that electron-equivalent energy units are used. Solid: $(M_\delta, \sigma_{\delta n}) = (52 \text{ GeV c}^{-2}, 7.2 \times 10^{-42} \text{ cm}^2)$, best fit to annual-modulation data alone. Dashed: $(M_\delta, \sigma_{\delta n}) = (44 \text{ GeV c}^{-2}, 5.4 \times 10^{-42} \text{ cm}^2)$, best fit to combined annual-modulation and 1996 exclusion-limit analysis. The energy resolution function has been convolved with the expected spectra.

is seen in calibration data taken with a ^{137}Cs source, which emits 662-keV photons (see Figure 11 of [150]). Multiple-scatter data are included in this calibration spectrum, but it is not expected that the single-scatter data shown in Figure E.1 should exhibit a significantly different spectrum. The efficiency-corrected background spectrum, Figure E.1, displays a flat counting rate above 5 keVee, a bump at 3.6 keVee that presumably is an X-ray peak, and then a falloff below 3.6 keVee that has the shape of the 3.6-keVee resolution function. No candidate for this peak is given. However, regardless of the source of the peak, the falloff below 3.6 keVee suggests a sharp dropoff in the true energy spectrum (before smearing by the detector-resolution function) at 3.6 keVee, which would be unphysical. The dropoff may indicate that the efficiency function shown in Figure E.2 is incorrect below 3.6 keVee. As is seen in Figure E.5, the majority of the annual-modulation signal is in the 2-to-4-keVee energy range, so such an error could be significant.

Second, the minimum- y WIMP mass and cross section derived by the above analyses do not appear to fit the “Figure 2” data reasonably. Figure E.6 shows the Figure 2 data with the expected annual-modulation signal for $(M_\delta, \sigma_{\delta n}) = (52 \text{ GeV c}^{-2}, 7.2 \times 10^{-42} \text{ cm}^2)$, which has amplitude $A = 0.0111 \text{ keV}^{-1} \text{ kg}^{-1} \text{ d}^{-1}$. Recall that the Figure 2 data is the modulated counting rate averaged between 2 and 6 keVee. Figure E.6 also shows the expected signal for $(M_\delta, \sigma_{\delta n}) = (44 \text{ GeV c}^{-2}, 5.4 \times 10^{-42} \text{ cm}^2)$, which has $A = 0.0038 \text{ keV}^{-1} \text{ kg}^{-1} \text{ d}^{-1}$. It is clear that neither of these amplitudes fits the Figure 2 data well. The best-fit amplitude for the Figure 2 data is $A = 0.0221 \text{ keV}^{-1} \text{ kg}^{-1} \text{ d}^{-1}$ and is shown in Figure E.6. Formally, the χ^2 of the two annual-modulation amplitudes $A = 0.0111 \text{ keV}^{-1} \text{ kg}^{-1} \text{ d}^{-1}$ and $A = 0.0038 \text{ keV}^{-1} \text{ kg}^{-1} \text{ d}^{-1}$ are 29.0 and 31.6, respectively. There are 20 data points, but, the modulation amplitude and mean count

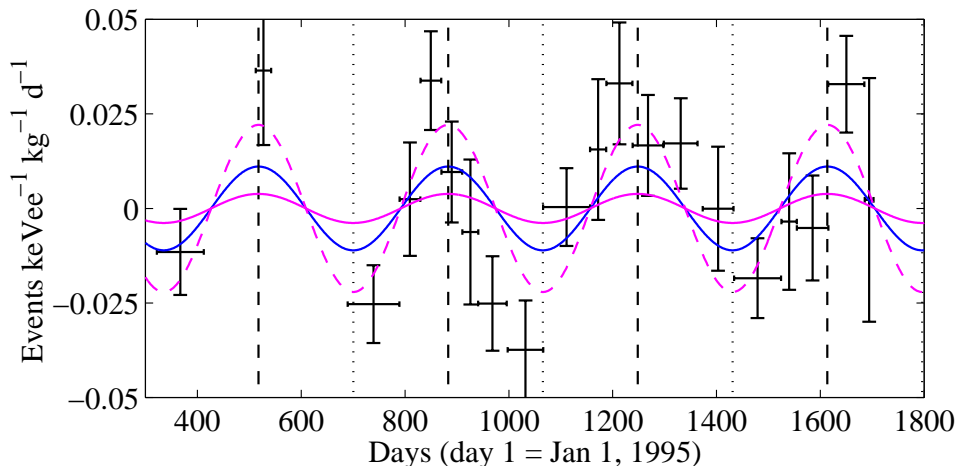


Figure E.6: DAMA modulated event rate vs. time with expected annual-modulation signals superimposed. The data are the same as Figure E.3, though the vertical axis limits have been changed. Light dashed (top): modulation amplitude that best fits these data alone, $A = 0.0221 \text{ keV}^{-1} \text{ kg}^{-1} \text{ d}^{-1}$. Dark solid (middle): modulation amplitude corresponding to $(M_\delta, \sigma_{\delta n}) = (52 \text{ GeV c}^{-2}, 7.2 \times 10^{-42} \text{ cm}^2)$, the minimum- y WIMP mass and cross section for the analysis of the annual-modulation data alone, with $A = 0.0111 \text{ keV}^{-1} \text{ kg}^{-1} \text{ d}^{-1}$. Light solid (bottom): modulation amplitude corresponding to $(M_\delta, \sigma_{\delta n}) = (44 \text{ GeV c}^{-2}, 5.4 \times 10^{-42} \text{ cm}^2)$, the minimum- y WIMP mass and cross section from combined analysis of the annual-modulation data and the 1996 pulse-shape-analysis exclusion limit, with $A = 0.0038 \text{ keV}^{-1} \text{ kg}^{-1} \text{ d}^{-1}$.

rate are nominally determined from the data. Two separate means are calculated, one for the first year and a second for the remaining three years [87]. Thus, there are 17 degrees of freedom. The resulting χ^2 percentiles are 96.6% and 98.3%. This level of disagreement is troubling. Furthermore, in the paper, the χ^2 percentiles are calculated erroneously by assuming 20 degrees of freedom.

Presumably, the discrepancy between the annual-modulation amplitude expected from the minimum- y analyses and the simple fit to the Figure 2 data arises from the $b_{jk} \geq 0$ constraint: a WIMP with cross section that fits the Figure 2 data well yields DC WIMP event rates larger than the observed total event rates. This reinforces the criticism of the shape of DC background spectrum made above — it drops too quickly below 3 keV, which is presumably where the constraint has the largest effect.

Third, there appears to be a problem with the energy spectrum of the annual modulation. Though no energy spectrum of the modulated signal is available in [88], it is noted that, if the 5–6-keV bin is discarded in calculating the Figure 2 data, the χ^2 of the Figure 2 data with respect to the expected annual-modulation signals improve to 11.5 and 12.3 for the analyses with and without the 1996 limit, respectively. The corresponding χ^2 percentiles, assuming 17 degrees of freedom, are 17.1% and 21.8%, respectively. Though a plot analogous to Figure E.3 without the 5–6-keV data is not given, one can easily infer that the modulation amplitude of the data must decrease significantly when the 5–6-keV bin is discarded in order to reduce the χ^2 by these large amounts. This is disturbing — a significant fraction of the annual-modulation signal appears to be in the

5–6-keV bin, where Figure E.5 indicates there should be negligible signal.

E.4 Compatibility Analysis of the DAMA and CDMS Results

Though there are a number of reasons to doubt the DAMA claim, it is also useful to perform an analysis of the compatibility of the CDMS and DAMA results, taking the latter at face value. It is intuitively clear from Figure E.4 that the CDMS data are not compatible with the DAMA annual-modulation claim. Though the CDMS data do not exclude the entire DAMA contour at 90% CL, it must be remembered that the DAMA contour is a 3σ CL contour, corresponding asymptotically to a 98.9% CL allowed region. The two experiments are clearly out on the tails of each other's likelihood functions. In this section, the compatibility of the two experiments is evaluated in both heuristic and rigorous ways.

In making the comparison, it is important to compare to the appropriate version of the DAMA result. The CDMS data are fully compatible with the DAMA 1996 exclusion limit, as is clear from Figure E.4. There is no need to test this. Therefore, the comparison should be made with the DAMA annual-modulation analysis alone. Clearly, comparison with the combined DAMA analysis would yield a higher level of compatibility, but this is because the inclusion of the 1996 exclusion limit dilutes the test.

Heuristically, the compatibility of the two data sets can be checked by simply plotting the recoil-energy spectrum expected for various points in the DAMA 3σ CL allowed region over the CDMS recoil-energy spectrum. This is done in Figure E.7, correcting the WIMP spectra for the CDMS efficiency function. The left plot shows the spectrum expected for the DAMA minimum- y point at $(52 \text{ GeV c}^{-2}, 7.2 \times 10^{-42} \text{ cm}^2)$. Clearly, it is very inconsistent, and, as indicated Figure E.4, it is ruled at $> 90\%$ CL. The second spectrum shown in the left plot of Figure E.7 corresponds to $(40 \text{ GeV c}^{-2}, 2.3 \times 10^{-42} \text{ cm}^2)$, the lowest cross-section point of the DAMA 3σ CL region. It is reasonably consistent with the observed spectrum.

However, comparison to the CDMS recoil-energy spectrum does not account for the neutron component of CDMS nuclear recoils. The right plot of Figure E.7 shows a “background-subtracted” spectrum, where the neutron background has been normalized to the value that best fits the CDMS data, $n = 17.5$ events (see Section 8.3), and subtracted from the observed spectrum. This background-subtracted spectrum is fairly inconsistent with even the $(40 \text{ GeV c}^{-2}, 2.3 \times 10^{-42} \text{ cm}^2)$ point, though not at 90% CL. CDMS excludes this point at only 75%. Finally, for completeness, the right plot of Figure E.7 also shows a WIMP spectrum corresponding to the lowest cross-section point of the DAMA combined analysis 3σ CL contour, at about $(40 \text{ GeV c}^{-2}, 1.2 \times 10^{-42} \text{ cm}^2)$. This point is consistent with the CDMS data. This is not surprising, given that this point is well below the CDMS 90% CL exclusion limit.

The compatibility of the CDMS and DAMA results can be tested rigorously by a likelihood-ratio test. This is similar the likelihood-ratio tests done in Chapter 8. The two hypotheses are that the CDMS and DAMA data are derived from the same WIMP mass and cross section or from different WIMP masses and cross sections. The likelihood ratio is

$$R = \frac{\mathcal{L}_C(X_C|\widehat{M}_\delta, \widehat{\sigma}_{\delta n})\mathcal{L}_D(X_D|\widehat{M}_\delta, \widehat{\sigma}_{\delta n})}{\mathcal{L}_C(X_C|\widehat{M}_{\delta C}, \widehat{\sigma}_{\delta n C})\mathcal{L}_D(X_D|\widehat{M}_{\delta D}, \widehat{\sigma}_{\delta n D})} \quad (\text{E.4})$$

where \mathcal{L}_C is the CDMS likelihood function evaluated for the CDMS data X_C and \mathcal{L}_D is the DAMA

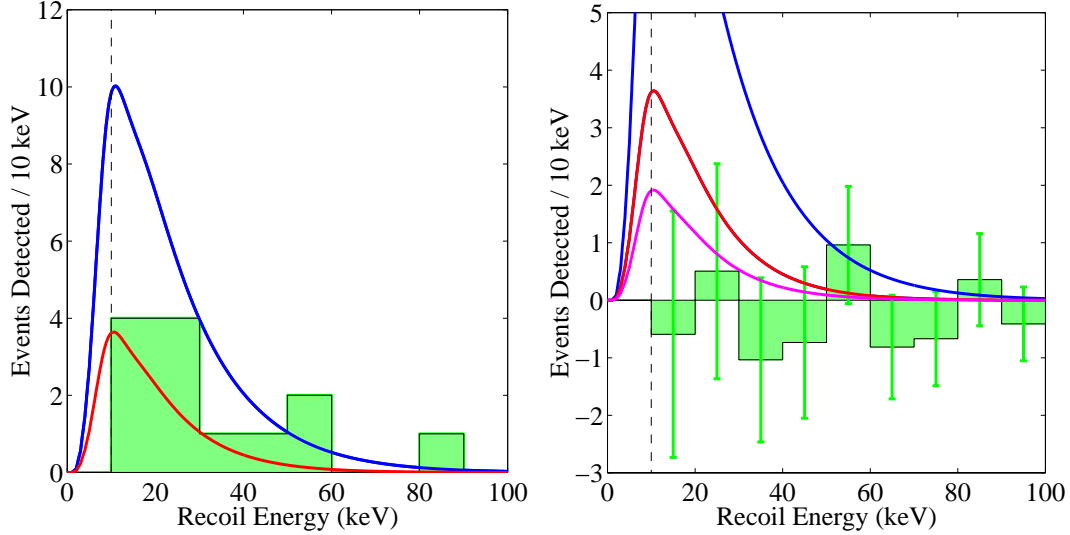


Figure E.7: Comparison of CDMS nuclear-recoil energy spectrum with that expected for the WIMP model that best fits the DAMA data. Left: comparison to full CDMS nuclear-recoil spectrum (13 events). Top curve: DAMA annual-modulation analysis minimum- y point at $(52 \text{ GeV c}^{-2}, 7.2 \times 10^{-42} \text{ cm}^2)$. Bottom curve: lowest cross-section point of DAMA annual-modulation 3σ CL allowed region. Right: “background-subtracted” CDMS nuclear-recoil energy spectrum. Top two curves are the same as in the left plot. The bottom curve corresponds to $(40 \text{ GeV c}^{-2}, 1.2 \times 10^{-42} \text{ cm}^2)$, the lowest cross-section of the 3σ CL contour of the DAMA combined analysis. Figures provided by R. Schnee.

likelihood function evaluated for the DAMA data X_D . The numerator evaluates the combined likelihood function at the WIMP mass and cross section $(\widehat{M}_\delta, \widehat{\sigma}_{\delta n})$ that maximizes the combined likelihood. The denominator evaluates the likelihood functions at their separate maximum-likelihood masses and cross sections $(\widehat{M}_{\delta C}, \widehat{\sigma}_{\delta n C})$ and $(\widehat{M}_{\delta D}, \widehat{\sigma}_{\delta n D})$ and takes the product. R is bounded above by 1. The larger R is, the more compatible the two experiments are. In the asymptotic limit, where both likelihood functions are products of Gaussian probability functions, $-2 \log R$ is distributed as χ^2 for two degrees of freedom. The asymptotic limit does not hold here, especially for the CDMS data, but Monte Carlo calculation of the expected distribution of R is computationally intractable because both experiments must be simulated over a large area in the plane of WIMP mass and cross section. Therefore, the asymptotic limit is used as an indication of the level of compatibility.

The full DAMA likelihood function is not available. However, it is straightforward to calculate a likelihood function using the Figure 2 data alone — the error bars are known. This disregards the $b_{jk} \geq 0$ constraint that forces the cross section down, but, as noted above, the large effect of this constraint is suspicious. Contours for the DAMA likelihood function calculated in this way are shown in Figure E.8. Clearly, the likelihood function moves higher in cross section because the $b_{jk} \geq 0$ constraint is not applied. The contours are not well localized in mass because no spectral information is available from the Figure 2 data.

A contour plot for the combined likelihood function (the numerator of R) is shown in

Figure E.9. The combined likelihood is maximized at $(42 \text{ GeV c}^{-2}, 4.9 \times 10^{-42} \text{ cm}^2)$. In the asymptotic limit, the CDMS data and the DAMA Figure 2 data are incompatible at $> 99.98\%$ CL: only 0.02% of experiments would have found lower values of R than the two data sets give. The actual confidence level should not be taken too seriously because the conditions for application of the asymptotic limit are not met. But, clearly the two experiments are very incompatible. This can be seen graphically with two plots: a comparison of the $(\widehat{M}_\delta, \widehat{\sigma}_{\delta n})$ annual-modulation amplitude to the DAMA Figure 2 data and the $(\widehat{M}_\delta, \widehat{\sigma}_{\delta n})$ recoil-energy spectrum to the background-subtracted CDMS data, shown in Figures E.10 and E.11. Clearly, the WIMP parameters that maximize the joint likelihood fit each experiment quite badly.

The incompatibility result is fairly robust. To be more generous, the likelihood function calculated by the above method can be scaled down in cross section so it approximately overlays the published DAMA 3σ CL contour (annual-modulation only), and this function used as an approximation to the true DAMA likelihood function (*i.e.*, including the $b_{jk} \geq 0$ constraint). When this is done, the new joint likelihood is maximized at $(42 \text{ GeV c}^{-2}, 4.2 \times 10^{-42} \text{ cm}^2)$. The incompatibility confidence level drops to 99.8% CL. Also, a reasonable criticism of the CDMS analysis is that too many Ge double-scatter nuclear recoils are seen as compared to the simulation. Discarding these events makes the CDMS data fully consistent with the simulation but also weakens the CDMS exclusion limit because the predicted neutron background is decreased. However, even after both discarding the multiples and shifting the likelihood contours down, the two experiments are still incompatible at 96.8% CL.

E.5 On Spin-Dependent WIMP Interactions

A final note — it may be possible to reconcile the CDMS and DAMA results if the signal seen by DAMA is due to WIMP scattering via spin-dependent interactions. Iodine and sodium both are mono-isotopic and odd- p nuclei, while the natural germanium used in the CDMS detectors has only a 7% abundance of the odd- n isotope ^{73}Ge (see Chapter 2 for a brief discussion of spin-dependent interactions). Thus, DAMA certainly would be more sensitive to a WIMP interacting primarily through spin-dependent interactions. It is difficult to compare the CDMS and DAMA data precisely for the spin-dependent case because nuclear-physics modeling is needed to relate the Na and I cross sections to a Ge cross section. Spin-dependent interactions may even render the DAMA data more internally consistent by modifying the annual-modulation spectrum relative to the DC WIMP-interaction spectrum. However, the spin-dependent cross section implied by the DAMA data is approximately a factor of 50 larger than is expected for MSSM WIMPs [151].

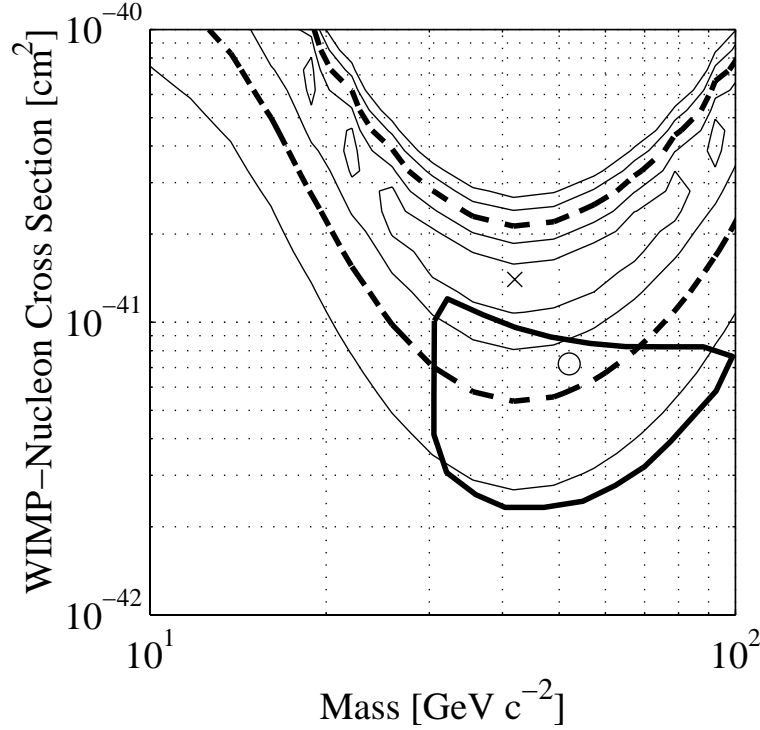


Figure E.8: DAMA log likelihood function calculated from Figure 2 data (*i.e.*, no spectral information, $b_{jk} \geq 0$ constraint not applied). The contours indicate $\Delta \log \mathcal{L}_D = -0.5, -2, -4.5, -8$, and -12.5 , corresponding to $1\sigma, 2\sigma, 3\sigma, 4\sigma$, and 5σ contours. (The lower portion of the 5σ contour is not visible on the plot.) The thick dashed contour is $\Delta \log \mathcal{L}_D = -4.5$. The maximum likelihood point is $(42 \text{ GeV c}^{-2}, 1.4 \times 10^{-41} \text{ cm}^2)$, marked with a \times . The minimum- y point and 3σ CL contour determined by the DAMA annual-modulation analysis (without inclusion of the 1996 exclusion limit) are shown by the circle and the thick solid contour. The likelihood contours are not localized in WIMP mass because no spectral information is available from DAMA's Figure 2; the contours' shapes reflect the sensitivity of the 2-to-6-keVee bin as a function of M_δ .

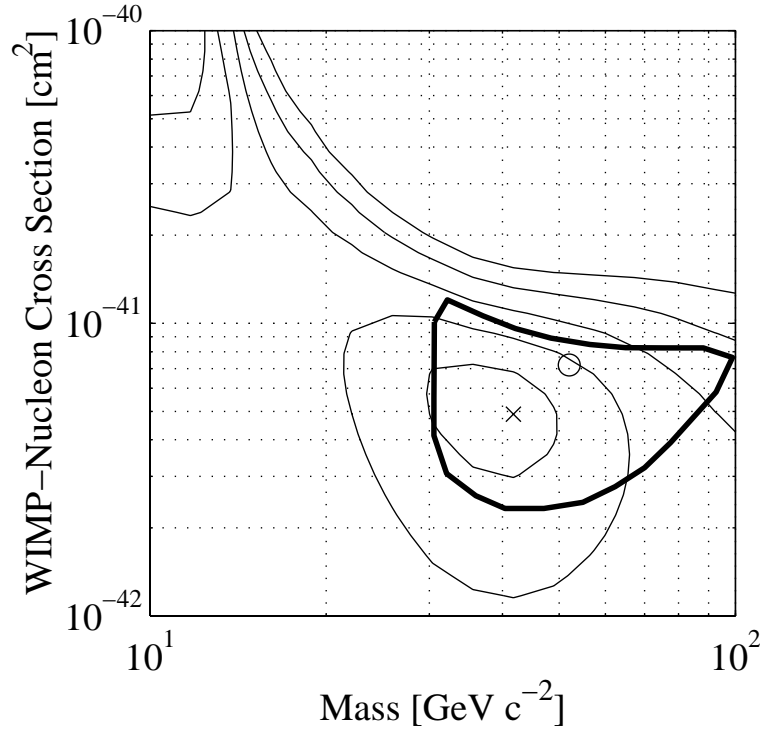


Figure E.9: Combined CDMS/DAMA log likelihood function $\log(\mathcal{L}_C \mathcal{L}_D)$ in the $(M_\delta, \sigma_{\delta n})$ plane. The contours indicate $\Delta \log(\mathcal{L}_C \mathcal{L}_D) = -0.5, -2, -4.5, -8$, and -12.5 , corresponding to $1\sigma, 2\sigma, 3\sigma, 4\sigma$, and 5σ contours (note that these contours have nothing to do with the compatibility CL!). The \times indicates the joint maximum-likelihood $(\widehat{M}_\delta, \widehat{\sigma}_{\delta n})$ at $(42 \text{ GeV c}^{-2}, 4.9 \times 10^{-42} \text{ cm}^2)$. The minimum- y point and 3σ CL contour determined from by the DAMA annual-modulation analysis (without inclusion of the 1996 exclusion limit) are shown by the circle and the thick solid contour.

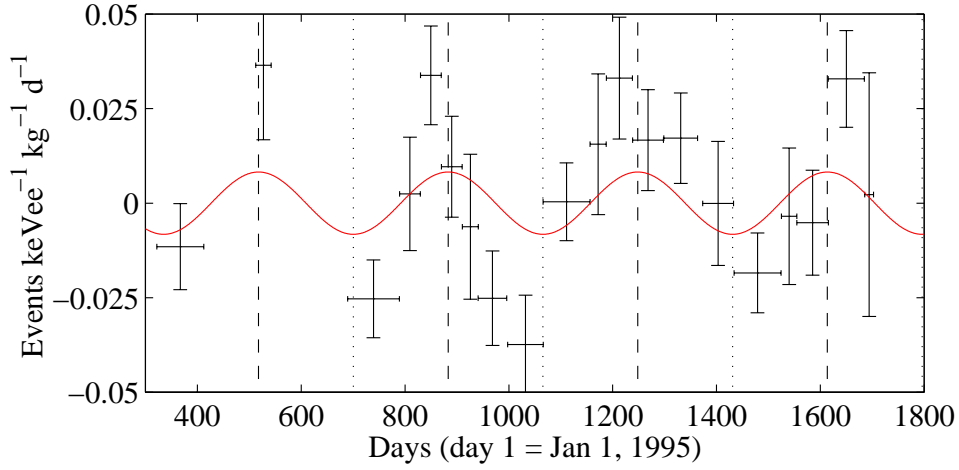


Figure E.10: Comparison of DAMA Figure 2 data to the annual-modulation signal expected for the WIMP that maximizes the joint CDMS/DAMA likelihood. The annual-modulation amplitude $A = 0.0082 \text{ keV}^{-1} \text{ kg}^{-1} \text{ d}^{-1}$ is shown for a WIMP with mass and cross section $(\widehat{M}_\delta, \widehat{\sigma}_{\delta n}) = (42 \text{ GeV c}^{-2}, 4.9 \times 10^{-42} \text{ cm}^2)$.

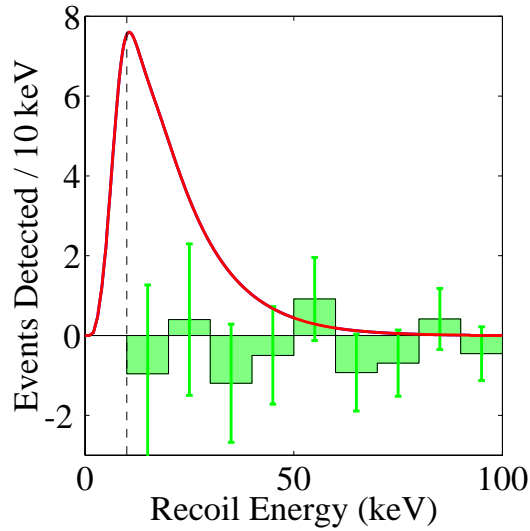


Figure E.11: Comparison of CDMS recoil-energy spectrum to that expected for the WIMP that maximizes the joint CDMS/DAMA likelihood. The background-subtracted CDMS spectrum is shown with the spectrum expected for a WIMP with mass and cross section $(\widehat{M}_\delta, \widehat{\sigma}_{\delta n}) = (42 \text{ GeV c}^{-2}, 4.9 \times 10^{-42} \text{ cm}^2)$. Figure provided by R. Schnee.

Bibliography

- [1] P. J. E. Peebles, *Principles of Physical Cosmology* (Princeton University Press, Princeton, NJ, 1993).
- [2] E. W. Kolb and M. S. Turner, *The Early Universe* (Addison-Wesley, Reading, MA, 1990).
- [3] M. S. Turner and J. A. Tyson, *Rev. Mod. Phys.* **71**, 145 (1999).
- [4] P. Salucci and M. Persic, in *ASP Conf. Ser. 117: Dark and Visible Matter in Galaxies and Cosmological Implications* (Brigham Young University, Provo, UT, 1997), pp. 1–27.
- [5] D. S. Davis and R. E. White, *Astrophys. J. Lett.* **470**, L35 (1996).
- [6] M. Loewenstein and R. E. White, *Astrophys. J.* **518**, 50 (1999).
- [7] M. Persic, P. Salucci, and F. Stel, *Mon. Not. Roy. Astron. Soc.* **281**, 27 (1996).
- [8] A. H. Sonnenschein, Ph.D. thesis, University of California, Santa Barbara, 1999.
- [9] J. Binney and S. Tremaine, *Galactic Dynamics* (Princeton University Press, Princeton, NJ, 1987).
- [10] M. Girardi *et al.*, *Astrophys. J.* **505**, 74 (1998).
- [11] M. Girardi *et al.*, *Astrophys. J.* **530**, 62 (2000).
- [12] D. A. White, C. Jones, and W. Forman, *Mon. Not. Roy. Astron. Soc.* **292**, 419 (1997).
- [13] M. Bartelmann and P. Schneider, astro-ph/9912508, to appear in *Phys. Rep.*
- [14] J. E. Carlstrom *et al.*, astro-ph/9905255.
- [15] B. S. Mason and S. T. Myers, astro-ph/9910438.
- [16] T. Padmanabhan, *Structure Formation in the Universe* (Cambridge University Press, Cambridge, 1993).
- [17] E. Hivon, private communication.
- [18] E. Torbet *et al.*, *Astrophys. J. Lett.* **521**, L79 (1999).
- [19] A. D. Miller *et al.*, *Astrophys. J. Lett.* **524**, L1 (1999).

- [20] P. D. Mauskopf *et al.*, astro-ph/9911444.
- [21] K. Coble *et al.*, *Astrophys. J. Lett.* **519**, L5 (1999).
- [22] J. B. Peterson *et al.*, *Astrophys. J. Lett.* **532**, L83 (2000).
- [23] S. Dodelson and L. Knox, *Phys. Rev. Lett.* **84**, 3523 (2000).
- [24] P. de Bernardis *et al.*, *Nature* **404**, 955 (2000).
- [25] S. Hanany *et al.*, astro-ph/0005123.
- [26] L. Knox and L. Page, astro-ph/0002162.
- [27] M. Harwit, *Astrophysical Concepts* (Springer-Verlag, New York, 1988).
- [28] M. Hamuy *et al.*, *Astron. J.* **112**, 2391 (1996).
- [29] S. Perlmutter *et al.*, in *Thermonuclear Supernovae, NATO ASI* (Kluwer Academic Publishers, Dordrecht, 1997), p. 749.
- [30] A. G. Riess, W. H. Press, and R. P. Kirshner, *Astrophys. J.* **473**, 88 (1996).
- [31] S. Perlmutter *et al.*, *Astrophys. J.* **517**, 565 (1999).
- [32] A. G. Riess *et al.*, *Astron. J.* **116**, 1009 (1998).
- [33] A. Aguirre, *Astrophys. J.* **525**, 583 (1999).
- [34] N. A. Bahcall, X. Fan, and R. Cen, *Astrophys. J. Lett.* **485**, L53 (1997).
- [35] A. Dekel, astro-ph/9911501.
- [36] D. Tytler, J. M. O'Meara, N. Suzuki, and D. Lubin, astro-ph/0001318, to appear in *Phys. Scr.*
- [37] E. Gawiser and J. Silk, *Science* **280**, 1405 (1998).
- [38] D. H. Weinberg, J. Miralda-Escudé, L. Hernquist, and N. Katz, *Astrophys. J.* **490**, 564 (1997).
- [39] C. Flynn, A. Gould, and J. N. Bahcall, *Astrophys. J. Lett.* **466**, L55 (1996).
- [40] C. Alcock *et al.*, astro-ph/0001272.
- [41] B. D. Fields, K. Freese, and D. S. Graff, *New Astron.* **3**, 347 (1998).
- [42] D. S. Graff, K. Freese, T. P. Walker, and M. H. Pinsonneault, *Astrophys. J. Lett.* **523**, L77 (1999).
- [43] B. D. Fields, K. Freese, and D. S. Graff, *Astrophys. J.* **534**, 265 (2000).
- [44] R. Cen and J. P. Ostriker, *Astrophys. J.* **514**, 1 (1999).

- [45] B. J. Carr and J. H. MacGibbon, Phys. Rep. **307**, 141 (1998).
- [46] K. Jedamzik, Phys. Rep. **307**, 155 (1998).
- [47] C. Hagmann *et al.*, Phys. Rev. Lett. **80**, 2043 (1998).
- [48] C. Athanassopoulos *et al.*, Phys. Rev. Lett. **81**, 1774 (1998).
- [49] K. Eitel, New J. Phys. **2**, 1 (2000).
- [50] A. O. Bazarko, hep-ex/9906003.
- [51] M. Drees, hep-ph/9911409.
- [52] F. Wilczek, hep-ph/0002045.
- [53] L. Girardello and M. Grisaru, Nucl. Phys. B **194**, 65 (1982).
- [54] G. Jungman, M. Kamionkowski, and K. Griest, Phys. Rep. **267**, 195 (1996).
- [55] L. Bergström, P. Ullio, and J. H. Buckley, Astropart. Phys. **9**, 137 (1998).
- [56] D. D. Dixon *et al.*, New Astron. **3**, 539 (1998).
- [57] P. Gondolo, astro-ph/9807347.
- [58] J. Ellis, T. Falk, G. Gani, and K. A. Olive, hep-ph/0004169.
- [59] L. Bergström, J. Edsjö, and P. Gondolo, Phys. Rev. D **58**, 103519/1 (1998).
- [60] J. M. Losocco *et al.*, Phys. Lett. B **188**, 388 (1987).
- [61] M. M. Boliev *et al.*, Nucl. Phys. B Proc. Supp. **48**, 83 (1996).
- [62] N. Sato *et al.*, Phys. Rev. D **44**, 2220 (1991).
- [63] M. Mori *et al.*, Phys. Lett. B **270**, 89 (1991).
- [64] M. Mori *et al.*, Phys. Lett. B **289**, 463 (1992).
- [65] M. Ambrosio *et al.*, astro-ph/0002492.
- [66] P. Gondolo and J. Silk, Phys. Rev. Lett. **83**, 1719 (1999).
- [67] A. M. Ghez, B. L. Klein, M. Morris, and E. E. Becklin, Astrophys. J. **509**, 678 (1998).
- [68] R. Genzel, A. Eckart, T. Ott, and F. Eisenhauer, Mon. Not. Roy. Astron. Soc. **291**, 219 (1997).
- [69] P. Gondolo, hep-ph/0002226.
- [70] S. Orito *et al.*, Phys. Rev. Lett. **84**, 1078 (2000).
- [71] L. Bergström, J. Edsjö, and P. Ullio, Astrophys. J. **526**, 215 (1999).

- [72] S. Coutu *et al.*, *Astropart. Phys.* **11**, 429 (1999).
- [73] S. W. Barwick *et al.*, *Phys. Rev. Lett.* **75**, 390 (1995).
- [74] M. W. Goodman and E. Witten, *Phys. Rev. D* **31**, 3059 (1985).
- [75] A. Drukier and L. Stodolsky, *Phys. Rev. D* **30**, 2295 (1984).
- [76] H.-Y. Cheng, hep-ph/0002157.
- [77] J. D. Lewin and P. F. Smith, *Astropart. Phys.* **6**, 87 (1996).
- [78] J. Edsjö and P. Gondolo, *Phys. Rev. D* **56**, 1879 (1997).
- [79] A. Corsetti and P. Nath, hep-ph/0003186.
- [80] R. J. Gaitskell and V. Mandic, Dark Matter Tools Working Group limit plotter, <http://dmtools.berkeley.edu/limitplots>.
- [81] D. O. Caldwell *et al.*, *Phys. Rev. Lett.* **61**, 510 (1988).
- [82] R. J. Gaitskell *et al.*, *Nucl. Phys. B Proc. Supp.* **51**, 279 (1996).
- [83] G. J. Feldman and R. Cousins, *Phys. Rev. D* **57**, 3873 (1998).
- [84] L. Baudis *et al.*, *Phys. Rev. D* **59**, 022001/1 (1999).
- [85] S. Ahlen *et al.*, *Phys. Lett. B* **195**, 603 (1987).
- [86] A. Morales *et al.*, hep-ex/0002053, submitted to *Phys. Lett. B*.
- [87] R. J. Gaitskell, private communication.
- [88] R. Bernabei *et al.*, INFN/AE-00/01.
- [89] N. J. C. Spooner, *Phys. Rep.* **307**, 253 (1998).
- [90] D. Snowden-Ifft, C. Martoff, and J. Burwell, *Phys. Rev. D* **61**, 101301/1 (2000).
- [91] A. Da Silva, Ph.D. thesis, University of British Columbia, 1996.
- [92] P. D. Barnes, Jr., Ph.D. thesis, University of California, Berkeley, 1996.
- [93] T. A. Perera, Ph.D. thesis, Case Western Reserve University, in preparation.
- [94] R. P. Kokoulin and A. A. Petrukhin, *Acta Phys. Acad. Sc. Hung.* **29**, 277 (1970).
- [95] T. Murota, A. Ueda, and H. Tanaka, *Prog. Theor. Phys.* **16**, 482 (1956).
- [96] T. A. Perera, private communication.
- [97] E. Segré, *Nuclei and Particles: An Introduction to Nuclear and Subnuclear Physics* (W. A. Benjamin, Reading, MA, 1980).

- [98] F. Khalchukov *et al.*, *Il Nuovo Cim.* **18C**, 517 (1995).
- [99] J. C. Barton, in *19th Intern. Cosmic Ray Conf.* (Scientific and Technical Information Branch, NASA, Washington, D.C., 1985), Vol. 8, pp. 98–101.
- [100] T. Florkowski, L. Morawska, and K. Rozanski, *Nucl. Geophys.* **2**, 1 (1988).
- [101] F. Khalchukov, A. Mal'gin, V. Ryassny, and O. Ryazhskaya, *Il Nuovo Cim.* **6C**, 320 (1983).
- [102] R. M. Clarke, Ph.D. thesis, Stanford University, 1999.
- [103] R. Abusaidi *et al.*, in preparation.
- [104] CDMS Collaboration, “Cold Hardware Review”, CDMSNote/0004002.
- [105] N. Wang, Ph.D. thesis, University of California, Berkeley, 1991.
- [106] T. A. Shutt, Ph.D. thesis, University of California, Berkeley, 1993.
- [107] A. K. Cummings, Ph.D. thesis, University of California, Berkeley, 1997.
- [108] W. K. Stockwell, Ph.D. thesis, University of California, Berkeley, 1996.
- [109] T. Shutt, “Selected Plots from the CDMS Presentation at the December 1996 Texas Astrophysics Meeting”, CDMS internal note, Jan. 1997.
- [110] R. J. Gaitskell, CDMSNote/9703002.
- [111] S. R. Golwala, CDMSNote/9708003.
- [112] D. S. Akerib *et al.*, *Nucl. Phys. B Proc. Supp.* **70**, 64 (1999).
- [113] F. C. Wellstood, Ph.D. thesis, University of California, Berkeley, 1988.
- [114] B. Sadoulet *et al.*, *Physica B* **219**, 741 (1996).
- [115] InterFET Corp., “Junction Field Effect Transistors”, device IF4500, process NJ450L.
- [116] SUF Detector Log, Vol. 10, p. 88.
- [117] R. J. Gaitskell, CDMSNote/9711001.
- [118] BLIPs 1–2 UCB Test Facility Log, Vol. 3, p. 7.
- [119] B. Cabrera, “Electron-Phonon Scattering”, CDMS internal note, Jan. 1993.
- [120] BLIPs 3–6 UCB Test Facility Log, Vol. 2, pp. 74–98.
- [121] T. Shutt *et al.*, *Nucl. Instrum. Methods Phys. Res., Sect. A* **444**, 340 (2000).
- [122] B. S. Neganov and V. N. Trofimov, *JETP Lett.* **28**, 328 (1978).
- [123] P. N. Luke, *J. Appl. Phys.* **64**, 6858 (1988).

- [124] T. Shutt *et al.*, in *Proceedings of the Seventh International Workshop on Low Temperature Detectors* (Max Planck Institute of Physics, Munich, 1997), pp. 224–226.
- [125] R. Diaz, Undergraduate honors thesis, University of California, Berkeley, 1995.
- [126] T. Shutt, “Ionization contact studies update”, electronic mail, May 21, 1998.
- [127] P. N. Luke, private communication.
- [128] S. M. Sze, *Physics of Semiconductor Devices* (John Wiley and Sons, New York, 1981).
- [129] Edwards High Vacuum International, Apiezon Wax W40.
- [130] J. Emes, private communication.
- [131] SUF Detector Log, Vol. 10, pp. 45–84.
- [132] T. A. Perera and D. S. Akerib, CDMSNote/9808001.
- [133] CDMS electronics web site, http://cdms.berkeley.edu/cdms_restricted/electronics.
- [134] W. D. Greason, *Electrostatic Damage in Electronics: Devices and Systems* (John Wiley and Sons, New York, 1987).
- [135] D. S. Akerib *et al.*, Nucl. Instrum. Methods Phys. Res., Sect. A **400**, 181 (1997).
- [136] J. J. Bock, Ph.D. thesis, University of California, Berkeley, 1994.
- [137] S. White, “Request for Quote for Fabrication of CDMS Striplines”, submitted to Basic Electronics, Inc.
- [138] D. Yvon *et al.*, Nucl. Instrum. Methods Phys. Res., Sect. A **368**, 778 (1996).
- [139] P. Horowitz and W. Hill, *The Art of Electronics* (Cambridge University Press, Cambridge, 1989).
- [140] S. R. Golwala, “Anti-alias Filter Calculations”, CDMS electronics web site, http://cdms.berkeley.edu/cdms_restricted/electronics.
- [141] R. Schnee, private communication.
- [142] W. H. Press, S. A. Teukolsky, W. T. Vetterling, and B. P. Flannery, *Numerical Recipes in C: The Art of Scientific Computing* (Cambridge University Press, Cambridge, 1992).
- [143] W. Eadie *et al.*, *Statistical Methods in Experimental Physics* (North Holland, Amsterdam, 1971).
- [144] R. M. Clarke *et al.*, Appl. Phys. Lett. **76**, 2958 (2000).
- [145] R. Schnee, CDMSNote in preparation.
- [146] R. Bernabei *et al.*, Phys. Lett. B **389**, 757 (1996).

- [147] R. Abusaidi *et al.*, in preparation.
- [148] CDMS Collaboration, CDMS II Proposal, 1999.
- [149] R. J. Gaitskell, CDMSNote/9805001.
- [150] R. Bernabei *et al.*, Il Nuovo Cim. **112A**, 545 (1999).
- [151] V. Mandic, private communication.